Department of Physics and Astronomy

Heidelberg University

Master thesis

in Physics

submitted by

Paul Leonard Große-Bley

born in Cologne

2021

Universal Dynamics and Correlation Functions

of the Three-Dimensional Bose Gas

at a Nonthermal Fixed Point

This Master thesis has been carried out by Paul Leonard Große-Bley

at the

Kirchhoff-Institute for Physics

under the supervision of

Herrn Prof. Thomas Gasenzer

Universelle Dynamik und Korrelationsfunktionen des dreidimensionalen Bose Gases an einem nicht-thermischen Fixpunkt:

Um nicht-thermische Fixpunkte (NTFP) während der Relaxation des ultrakalten, weit aus dem Equilibrium gequenchten Bose Gases zu studieren, wurden numerische Simulationen des semi-klassischen Gross-Pitaevskii Models in der 'Truncated Wigner'-Näherung (TWA) verwendet. Indem die Änderung der Dynamik durch das Quenchen zu sehr kleinen Impuls-Skalen untersucht wurde, konnte eine mögliche Erklärung für das experimentell entdeckte, unerwartet langsame Skalierungsverhalten in Glidden et al. [2021] gefunden werden, welche die scheinbar anomalen kritischen Exponenten nicht auf einen anomalen NTFP zurückführt. Nachdem, wie in Kobayashi et al. [2021] beschrieben, viele Vortex-Ringe mit zufälligen Orientierungen und Positionen in einem Kondensat platziert wurden, konnte ein unerwartet schnelles Skalierungsverhalten ($\alpha \approx 2.4$, $\beta \approx 0.8$) bei späten Zeiten festgestellt werden. Jenes folgte auf ein unterschiedliches Skalierungsverhalten bei frühen Zeiten welches dem erwarteten Gaußschen Fixpunkt ($\alpha \approx 1.65$, $\beta \approx 0.55$) entspricht. Es wurden Feld-, Dichte- und Phasen-Korrelationsfunktionen berechnet und verglichen um die Rolle von Dichte-Fluktuationen am Gaußschen NTFP zu bestimmen. Auf Basis dieser Korrelatoren wurden verbundene 4-Punkt Korrelationsfunktionen direkt berechnet und, durch Mikheev et al. [2019] inspiriert, verbundene 2-, 4-, 6- und 8-Punkt Phasenwinkel-Korrelationsfunktionen indirekt berechnet, unter der Annahme, dass die Vortex-dominierte Dynamik durch eine niederenergetische, effektive Feldtheorie (EFT) des Phasenwinkels beschrieben werden kann.

Universal Dynamics and Correlation Functions of the Three-Dimensional Bose Gas at a Nonthermal Fixed Point:

To study nonthermal fixed points (NTFP) during the relaxation of the ultra-cold Bose gas quenched far out of equilibrium, numerical simulations of the semi-classical Gross-Pitaevskii model in the Truncated Wigner Approximation (TWA) are employed. By investigating the change in dynamics due to quenching to very small momentum scales, a possible explanation for the experimentally found, slower than expected scaling behavior in Glidden et al. [2021] is found, according to which the seemingly anomalous critical exponents do not correspond an anomalous NTFP. After placing many vortex rings with random orientations and positions in a condensate as described in Kobayashi et al. [2021], a faster than expected scaling behavior ($\alpha \approx 2.4$, $\beta \approx 0.8$) was observed at late times following behavior consistent with the expected Gaussian fixed point ($\alpha \approx 1.65$, $\beta \approx 0.55$) at earlier times. Field-, density- and phase correlation functions were calculated and compared to determine the role of density fluctuations at the Gaussian NTFP. Based on these, connected 4-point correlation functions were calculated directly and, inspired by Mikheev et al. [2019], connected 2-, 4-, 6- and 8-point phase-angle correlation functions were calculated indirectly under the assumption that a low-energy effective field theory (EFT) in the phase-angle is able to describe the vortex-dominated dynamics.

Contents

1 Introduction

Ultra-cold Bose gases are at the frontier of research into non-equilibrium quantum many-body physics. This regime, being probed by experiments around the globe like Glidden et al. [2021], Johnstone et al. [2019], Prüfer et al. [2018] in all kinds of configurations, shapes and initial conditions, gives rise to new classes of universal phenomena waiting to be charted and classified in terms of nonthermal fixed points (NTFP) of the configuration space. NTFP typically appear during the relaxation of an isolated Bose gas forming a Bose-Einstein condensate on the way to thermal equilibrium. This is accompanied by coarsening regions of coherent phase and vanishing (quasi-) topological excitations like solitons in one dimension, point-vortices in two dimensions and vortex-lines in three dimensions.

In this thesis, an ultra-cold Bose gas in three dimensions and without an internal (Spin-) degree of freedom will be probed and analyzed numerically. To accurately model a weakly interacting Bose gas in the limit of high occupation numbers, the truncated Wigner approximation (TWA) is used, yielding the Gross-Pitaevskii equation (GPE) as a semi-classical description. The GPE is integrated numerically in time using a pseudo-spectral split-step Fourier method starting from sampled initial conditions distributed around a far-from-equilibrium starting point in configuration space.

After the successful theoretical [Karl and Gasenzer, 2017] and experimental [Johnstone et al., 2019] demonstration of a strongly anomalous NTFP for the two-dimensional Bose gas due to vortex clustering, new experimental results [Glidden et al., 2021] suggest another anomalous NTFP for the three-dimensional Bose gas, which was not yet observed numerically. Therefore, the first goal of this thesis will be to reproduce these experimental results numerically. Second, the use of full and connected correlation functions shall be explored in the absence of any internal degrees of freedom complicating their analysis by the sheer number of combinations.

In the following a short introduction to the Wigner-Weyl formalism as the main ingredient of the TWA, as well as the GPE, its interpretation, vortex lines as its quasi-topological solutions and NTFPs will be given. In chapter 2 different far-from-equilibrium initial states will be introduced and the dynamics of their spectra analyzed for self-similar scaling. Furthermore, in **??** a host of correlation functions will be defined and analyzed in the presence of the Gaussian NTFP. At last there will be a synopsis in chapter 4, giving conclusions and an outlook to possible future research.

1.1 Wigner-Weyl Quantization

In order to motivate the truncated Wigner approximation (TWA), the Wigner-Weyl quantization will be introduced loosely following Polkovnikov [2010]. Phase-space formulations of quantum mechanics like the Wigner-Weyl quantization are equivalent to the well-known Schrödinger- and Heisenberg-pictures and give a full, probabilistic description. While the Wigner-Weyl quantization can be derived from Feynman's path integral formalism, here it will only be presented starting from the operator formalism in its coherent state form.

Given the annihilation operator $\hat{\psi}$ and the creation operator $\hat{\psi}^{\dagger}$ the canonical coherent state is defined as the eigenstate $|\psi\rangle$ of $\hat{\psi}$ such that

$$\hat{\psi}|\psi\rangle = \psi|\psi\rangle \tag{1.1}$$

with the complex eigenvalue ψ. The equivalent of an operator $\hat{\Omega}(\hat{\psi}, \hat{\psi}^{\dagger})$ in this formalism is called a Weyl symbol and is given by the Wigner transform

$$\Omega_W(\boldsymbol{\psi}, \boldsymbol{\psi}^*) \equiv \frac{1}{2^M} \int \mathrm{d}^M\eta \, \mathrm{d}^M\eta^* \left\langle \boldsymbol{\psi} - \frac{\boldsymbol{\eta}}{2} \right| \hat{\Omega}(\hat{\boldsymbol{\psi}}, \hat{\boldsymbol{\psi}}^{\dagger}) \left| \boldsymbol{\psi} + \frac{\boldsymbol{\eta}}{2} \right\rangle$$
$$\times \exp\left(-|\boldsymbol{\psi}|^2 - \frac{1}{4}|\boldsymbol{\eta}|^2 + \frac{1}{2}(\boldsymbol{\eta}^*\boldsymbol{\psi} - \boldsymbol{\eta}\boldsymbol{\psi}^*) \right). \tag{1.2}$$

Here, M is the number of single particle states in the system. Therefore, operators, states and eigenvalues are M-vectors, i.e. $\boldsymbol{\psi} = \{\psi_j\}_{j=1\dots M}$. Operators that are totally symmetric in the fields can be directly exchanged for their eigenvalues as the corresponding Weyl symbol. The symmetric ordering of an operator $\hat{\Omega}(\hat{\psi}, \hat{\psi}^{\dagger})$ is also called Weyl ordering and is denoted as $: \hat{\Omega}(\hat{\psi}, \hat{\psi}^{\dagger}) :_W$. To illustrate this, the Weyl symbol of the number operator $\hat{n} = \hat{\psi}^{\dagger}\hat{\psi}$ is $n_W = |\psi|^2 - 1/2$, but the Weyl symbol of the Weyl ordered operator $: \hat{n} :_W \equiv (\hat{\psi}^{\dagger}\hat{\psi} + \hat{\psi}\hat{\psi}^{\dagger})/2$ is just $|\psi|^2$. By construction, correlation functions calculated in the path integral formalism are also Weyl ordered.

The Weyl symbol of the density matrix $\hat{\varrho}$ is the so-called Wigner function $\mathcal{W}(\boldsymbol{\psi}, \boldsymbol{\psi}^*)$. It is of special importance, as it serves as the quasi-probability distribution:

$$\left\langle \hat{\Omega}(\hat{\boldsymbol{\psi}}, \hat{\boldsymbol{\psi}}^{\dagger}) \right\rangle = \int \mathrm{d}^M\psi \, \mathrm{d}^M\psi^* \, \Omega_W(\boldsymbol{\psi}, \boldsymbol{\psi}^*) \mathcal{W}(\boldsymbol{\psi}, \boldsymbol{\psi}^*) \tag{1.3}$$

What distinguishes $\mathcal{W}(\boldsymbol{\psi}, \boldsymbol{\psi}^*)$ from a proper probability distribution is that it is not necessarily positive-definite.

The Weyl symbol of the product of two operators is

$$(\Omega_1\Omega_2)_W = \Omega_{1,W} \exp\left(\frac{\Lambda}{2}\right) \Omega_{2,W}, \tag{1.4}$$

with the symplectic coherent state operator

$$\Lambda \equiv \sum_j \frac{\overleftarrow{\partial}}{\partial\psi_j} \frac{\overrightarrow{\partial}}{\partial\psi_j^*} - \frac{\overleftarrow{\partial}}{\partial\psi_j^*} \frac{\overrightarrow{\partial}}{\partial\psi_j}, \tag{1.5}$$

where the arrows above the derivatives mark the direction in which they act. Using this, the equivalent of the commutator is the coherent state Moyal bracket

$$([\Omega_1, \Omega_2])_W = \{\Omega_{1,W}, \Omega_{2,W}\}_{\text{MBC}} \equiv 2\,\Omega_{1,W} \sinh\left(\frac{\Lambda}{2}\right) \Omega_{2,W}. \tag{1.6}$$

When applying the Wigner transformation to both sides of the von Neumann equation

$$i\hbar\frac{\partial\hat{\rho}}{\partial t} = [\hat{H}, \hat{\rho}], \tag{1.7}$$

which describes quantum dynamics in the Schrödinger picture, one gets a master equation for the Wigner function:

$$i\hbar\dot{\mathcal{W}} = 2H_W \sinh\left(\frac{\Lambda}{2}\right) \mathcal{W}, \tag{1.8}$$

where H_W is the Weyl symbol of the Hamiltonian describing the system.

By expanding the hyperbolic sine one finds that the zeroth order term yields the classic Liouville equation while the following terms can be interpreted as quantum corrections, which in general do not have to be small. However, in the presence of high occupation numbers $|\psi| \gg 1$ (wave-limit), higher order terms become less important and truncating the expansion becomes a viable option for a semi-classical approximation. Truncating after the first order quantum correction is then called the truncated Wigner approximation (TWA).

1.2 The Gross-Pitaevskii Equation

After introducing the TWA, it will now be applied to the specific system in question by plugging the Bose gas Hamiltonian

$$\hat{H} = \int \mathrm{d}^3x\,\hat{\psi}^\dagger \left(\frac{\hbar^2}{2m}\vec{\nabla}^2 + V_{\text{ext}}(\vec{x}) + g\hat{\psi}^\dagger\hat{\psi}\right) \hat{\psi} \equiv \int \mathrm{d}^3x\,\hat{\psi}^\dagger \mathcal{K}\hat{\psi}, \tag{1.9}$$

with an external potential $V_{\text{ext}}(\vec{x})$ added for generality, into Equation 1.8. The resulting Fokker-Planck equation

$$i\hbar\frac{\partial\mathcal{W}}{\partial t} = \int \mathrm{d}^3x\,\left(-\frac{\delta}{\delta\psi(\vec{x})}\mathcal{K}\psi + \frac{1}{4}\frac{\delta^3}{\delta^2\psi\delta\psi^*}\psi\right) \mathcal{W} - \text{c.c.} \tag{1.10}$$

$$\approx \int \mathrm{d}^3x\,\frac{\delta}{\delta\psi(\vec{x})}\mathcal{K}\psi\mathcal{W} - \text{c.c.}, \tag{1.11}$$

where the TWA was applied to get rid of the third order functional derivatives, can be rewritten as a stochastic partial differential equation in ψ, which is equivalent to the non-linear Schrödinger or Gross-Pitaevskii equation (GPE) [Steel et al., 1998]:

$$i\hbar\frac{\partial}{\partial t}\psi(\vec{x}, t) = \left(\frac{\hbar^2}{2m}\vec{\nabla}^2 + V_{\text{ext}}(\vec{x}) + g\,|\psi(\vec{x}, t)|^2\right) \psi(\vec{x}, t). \tag{1.12}$$

In three-dimensional space the coupling constant g of the non-linearity can be related to the s-wave scattering-length a_S by

$$g = \frac{4\pi\hbar^2 a_S}{m}. \tag{1.13}$$

Given the average density $\rho = N/V$, where V is the simulated volume, the characteristic length scale of the GPE is the healing length

$$\xi \equiv \frac{\hbar}{\sqrt{2mg\rho}} \tag{1.14}$$

and the characteristic time scale can be taken to be $2m\xi^2/\hbar$. The characteristic momentum scale is therefore naturally the so-called healing momentum

$$k_\xi = \frac{\hbar}{\xi} = \sqrt{2mg\rho}. \tag{1.15}$$

Originally the GPE is used as the mean-field description of only the condensate mode of a Bose gas [Gross, 1961, Pitaevskii, 1961]. In the context of the TWA it instead describes the full matter field.

Substituting the Madelung transform $\psi(\vec{x}, t) = \sqrt{\rho(\vec{x}, t)}e^{i\theta(\vec{x}, t)}$ into the GPE, separating the real and imaginary part of the equation and identifying the velocity $\vec{v}(\vec{x}, t) = \frac{\hbar}{m}\vec{\nabla}\theta(\vec{x}, t)$, one finds

$$\frac{\partial}{\partial t}\rho = -\vec{\nabla}(\rho\vec{v}) \tag{1.16}$$

$$\frac{\partial}{\partial t}\vec{v} + (\vec{v}\cdot\vec{\nabla})\vec{v} = -\frac{1}{m\rho}\vec{\nabla}(P + P_{\mathrm{q}}) - \frac{1}{m}\vec{\nabla}V_{\mathrm{ext}}, \tag{1.17}$$

where the quantum pressure $P_{\mathrm{q}} \equiv -\rho\frac{\hbar^2\vec{\nabla}^2}{4}\log\rho$ is expected to be insignificant at low energies, while the pressure $P \equiv \frac{g\rho^2}{2}$ arising from density interactions is dominating. These equations are the quantum analogue to the Euler equations of classical fluids. While the first equation is the continuity equation expressing the conservation of particle number (or mass), the second equation is concerned with momentum conservation. Conservation of total momentum is naturally only possible in the case of $V_{\mathrm{ext}} = 0$.

1.3 Universal Scaling

Starting from far-from-equilibrium initial states, one often finds that before finally thermalizing, the system approaches a non-thermal fixed point (NTFP). In the vicinity of that NTFP, one can observe a critical slowing down of the dynamics as well as local power laws in the angle-averaged occupation number spectrum

$$n(k, t) \equiv \frac{1}{4\pi}\int \mathrm{d}\Omega_k \langle\hat{\psi}^\dagger(\vec{k}, t)\hat{\psi}(\vec{k}, t)\rangle. \tag{1.18}$$

The power laws then show self-similar scaling in time as

$$n(k,t) = (t/t_0)^\alpha n((t/t_0)^\beta k, t_0), \tag{1.19}$$

where t_0 is an arbitrary reference time inside of the scaling time interval and α and β are critical exponents [Piñeiro Orioli et al., 2015]. Physically, this corresponds to a transport of particles to lower momentum scales, while energy is transported to higher momentum scales. There, a thermal tail k^{-2} develops long before the whole system thermalizes.

2 Initial States and Scaling

As calculating and sampling the Wigner distribution for any complex, non-equilibrium state is notoriously hard, the Wigner distribution is instead approximated by a independent Gaussian distribution for each mode. The Gaussian distributions are chosen to have the same first and second statistical moments as the Wigner distribution corresponding to a Fock states. This is accomplished by centering it around the number of particles in the Fock state using a standard deviation of $1/2$. In practice one takes a mean-field initial condition $\psi_0(\vec{k})$ and adds complex noise η which is normally distributed on both the real and imaginary axis independently, both with a mean of 0 and a standard deviation of $1/2$.
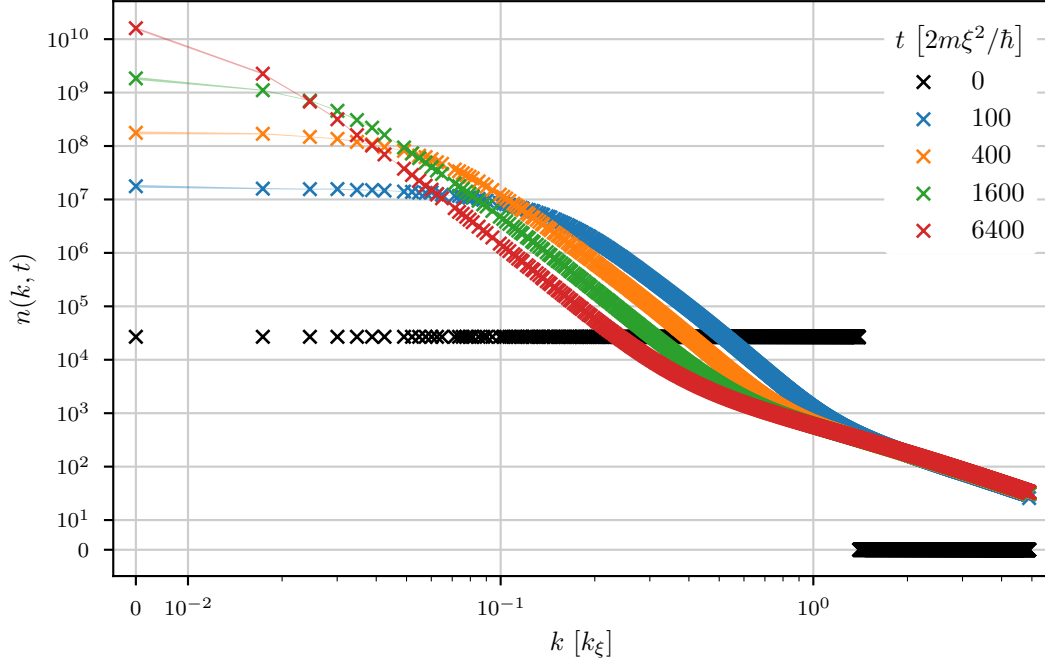
2.1 Box Initial State

The box initial condition as based on Piñeiro Orioli et al. [2015] is used as a well known reference initial condition, which is found to reliably lead to the Gaussian NTFP. To introduce dynamic instabilities, only modes $\psi(\vec{k}) = \sqrt{n(\vec{k})}e^{i\theta(\vec{k})}$ up to the cutoff momentum k_{cutoff} are occupied:

$$n(\vec{k}) = \frac{N}{\int \mathrm{d}^3k' \, \Theta(k_{\text{cutoff}} - |\vec{k}'|)} \Theta(k_{\text{cutoff}} - |\vec{k}|). \tag{2.1}$$

Here, Θ is the Heaviside step function and the cutoff momentum k_{cutoff} is usually chosen to be the inverse 'coherence length' $Q \equiv \sqrt{2}k_\xi$. The phase-angle $\theta(\vec{k})$ is chosen randomly from a uniform distribution over the range $[0, 2\pi)$. The used initial state differs from the cited one in including the condensate mode $\psi(\vec{k} = \vec{0})$ in the 'box', which is not observed to affect the dynamics in the universal regime. While such an idealized cutoff can not be achieved experimentally during a strong cooling quench, the dynamics in the universal regime are independent of the form of any power law tail between the over-occupied IR modes and the unoccupied UV modes in the initial distribution, as long as the power law is steep enough [Nowak et al., 2014].

The spectrum of this reference initial state can be found in Figure 2.1a. Relying on the fitting procedure described in Piñeiro Orioli et al. [2015] (the only difference being that a time in the middle of the logarithmical time interval was taken to be the reference time), the universal exponents were found to be $\alpha = 1.68 \pm 0.06$ and $\beta = 0.56 \pm 0.03$. A rescaled spectrum can be found in Figure 2.3.
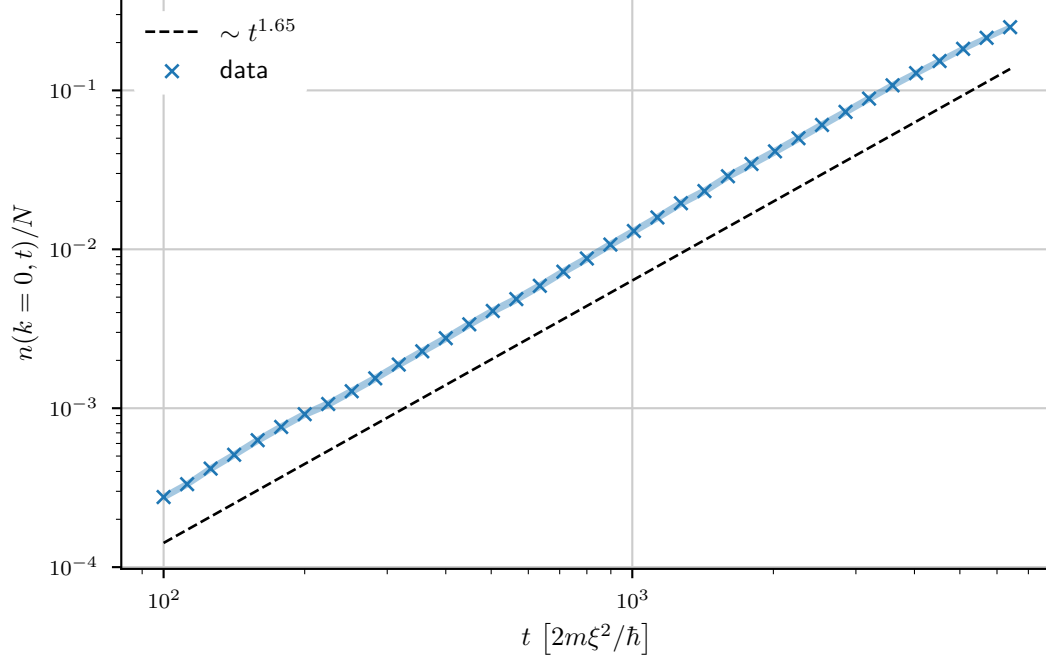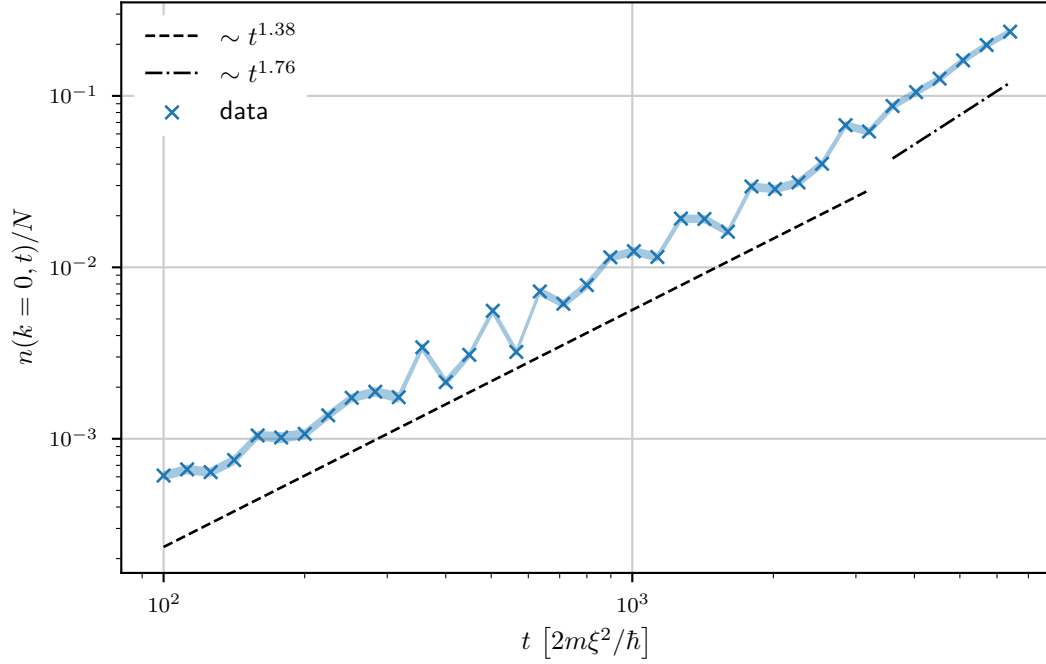
(a) $k_{\text{cutoff}} = 1.4k_\xi$
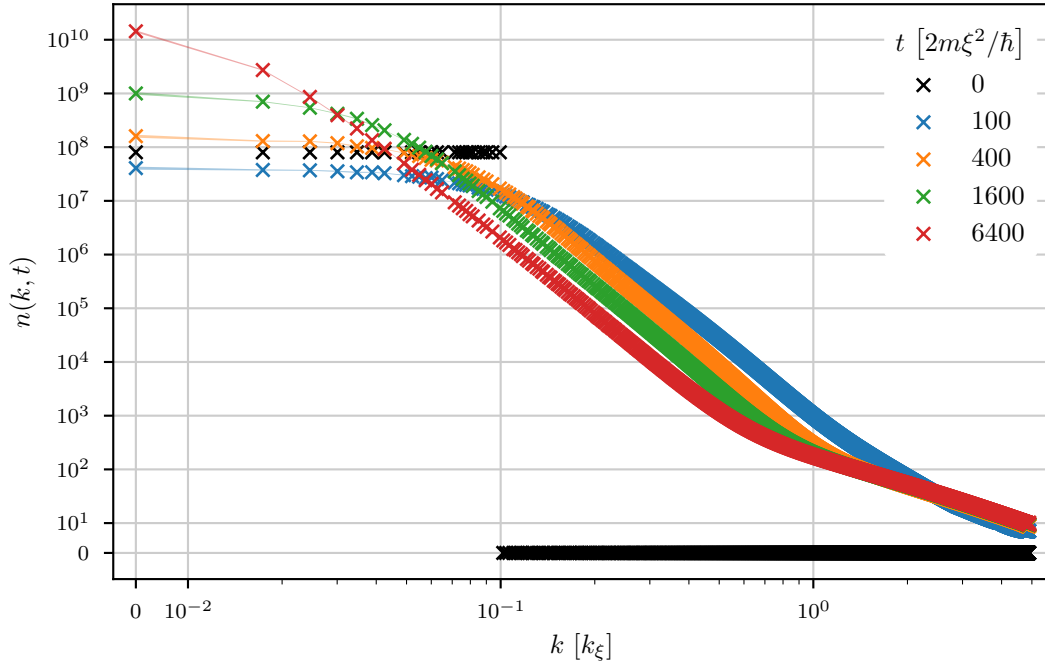
(b) $k_{\text{cutoff}} = 0.1k_\xi$

Figure 2.1: Angle-averaged occupation number spectrum of the box initial state with different k_{cutoff} and at logarithmically spaced times showing self-similar scaling. Both axes use logarithmic scales to visualize the scaling and power laws in momentum k but include a linear region around 0 to accommodate the condensate mode $k = 0$ and the empty UV-modes of the initial state. The error of n is estimated using bootstrap resampling and marked by a semi-transparent error band which is only visible as a line between the data points at low momenta.

(a) $k_{\text{cutoff}} = 1.4 k_\xi$

(b) $k_{\text{cutoff}} = 0.1 k_\xi$

Figure 2.2: Occupation number of the condensate mode of the box initial state with different k_{cutoff} and at logarithmically spaced times showing universal scaling. Both axes use logarithmic scales to visualize the scaling and power law in time t. The error of $n(0, t)$ is estimated using bootstrap resampling and marked by a semi-transparent error band.
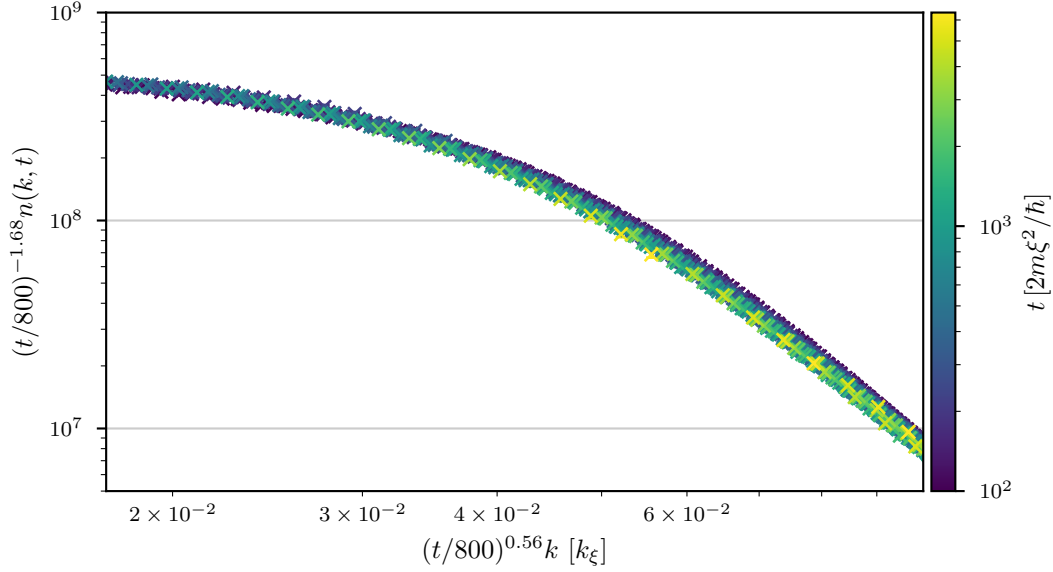
Figure 2.3: Log-log plot of the rescaled, angle-averaged occupation number spectrum in the k region used for fitting the universal exponents at logarithmically spaced times simulated from the box initial state with $k_{\text{cutoff}} = 1.4k_\xi$. The error of n is estimated using bootstrap resampling and marked by error bars.

2.1.1 Decreasing the Cutoff Momentum

When trying to reproduce the slow scaling found experimentally in Glidden et al. [2021] after a strong cooling quench, slow dynamics were observed when decreasing k_{cutoff} significantly below the inverse coherence length Q. As the fitted exponents α and β of the occupation number spectra like the ones pictured in Figure 2.1b are strongly dependent on the choice of time interval (See Figure 2.4), these dynamics might not actually represent universal scaling and therefore a new NTFP, but instead a very slow case of prescaling or a superposition of universal dynamics with non-universal phenomena. The problem becomes very clear with a look at the occupation number of the condensate mode in Figure 2.2b in comparison to the same plot for $k_{\text{cutoff}} = 1.4k_\xi$ in Figure 2.2a. While the condensate mode at $k_{\text{cutoff}} = 1.4k_\xi$ reflects the universal dynamics with $\alpha \approx 1.65$, the condensate mode at $k_{\text{cutoff}} = 0.1k_\xi$ shows significant and systematic oscillations. At late times, where the systems seems to enter an actual scaling regime, a scaling analysis of the spectrum is inhibited by the fact that the IR plateau is already below the finite momentum resolution of the simulation. These oscillations cause the dependence of fitted exponents on the choice of time interval and might be the cause of the seemingly slow scaling found experimentally as well. Due to the lack of information on the form of the initial state or approximate k_{cutoff} achieved by the experimental cooling quench it is not possible to come to a clear result in that regard.
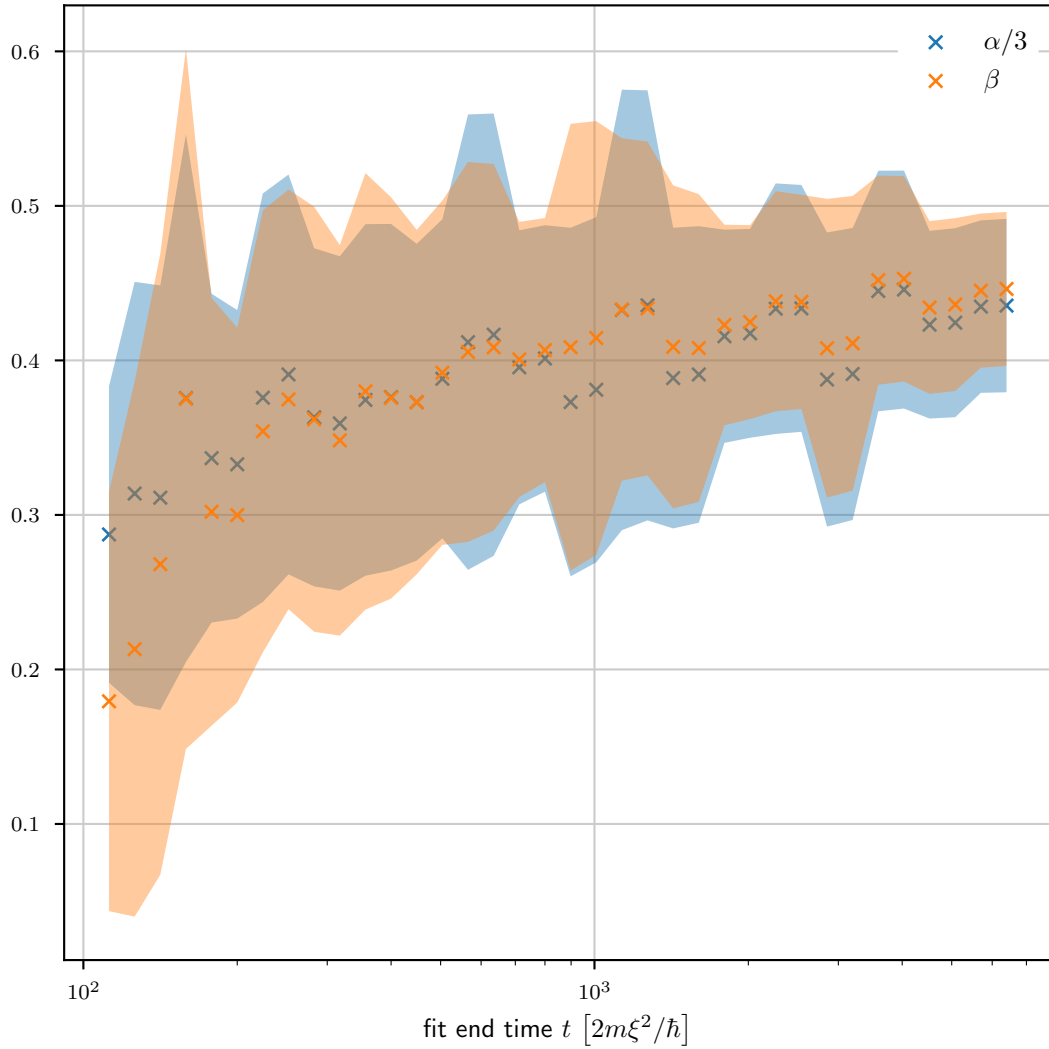
Figure 2.4: Fitted critical exponents α and β against the time of the latest occupation number spectrum used in the fit. Using only very early times it is possible to arrive at very small exponents.

2.2 Random Vortex Rings

Instead of designing the initial state around a given spectrum and generating vortices through instabilities, the random vortex rings (RVR) initial state as described in Kobayashi et al. [2021] consists of N_{v} big artificially placed vortex loops placed randomly on a condensate background. The vortex rings are all of the same radius R_{v} and to keep the total momentum of the system at zero, two rings of opposite circulation are placed on the lattice in parallel at a distance $d_{\mathrm{v}} = 2R_{\mathrm{v}}$. While the position of the vortex ring pair is chosen at random from a continuous uniform distribution over the full computational lattice, the orientation is chosen from a discrete uniform distribution over the six possible orientations along the three axes of the lattice. This particular configuration is rather easy to implement numerically while respecting the periodic boundary conditions. To add vortex rings to a condensate initial state, the Padé approximated form of single vortex ring ψ_{VR} is multiplied with the condensate wavefunction $\psi_0(\vec{x}) = \sqrt{\rho_0}\mathrm{e}^{\mathrm{i}\theta_0} = \text{const}$ in the center of the grid. Choosing the coordinate origin of x, y, z to be in the middle of the grid and the symmetry axis of the ring to be in the z-direction, as well as defining $r \equiv \sqrt{x^2 + y^2}$, the approximation of a single ring has the following form:

$$\psi_{\mathrm{VR}}(r, z, R) \equiv f\left(\sqrt{(r-R)^2 + z^2}\right) \exp\left(\mathrm{i}\arctan\left(\frac{z}{r-R}\right)\right), \tag{2.2}$$

$$f(d) \approx \sqrt{\frac{a_1(d/\xi)^2 + a_2(d/\xi)^4}{1 + b_1(d/\xi)^2 + a_2(d/\xi)^4}}, \tag{2.3}$$

$$a_1 \equiv \frac{73 + 3\sqrt{201}}{352}, \quad a_2 \equiv \frac{6 + \sqrt{201}}{528}, \quad b_1 \equiv \frac{21 + \sqrt{201}}{96}. \tag{2.4}$$

A ring of opposite circulation is achieved by taking the complex conjugate of this solution which corresponds to transforming $z \to -z$. Additionally, to help with the periodic boundary conditions, the long range effects of each vortex ring from the six 'neighboring volumes' are also multiplied with the condensate wave function:

$$\begin{aligned}
\psi_{\mathrm{VR}}(x, y, z, R) \to \ &\psi_{\mathrm{VR}}(x, y, z) \\
&\times \psi_{\mathrm{VR}}(L_x + x, y, z, R)\psi_{\mathrm{VR}}(-L_x + x, y, z, R) \\
&\times \psi_{\mathrm{VR}}(x, L_y + y, z, R)\psi_{\mathrm{VR}}(x, -L_y + y, z, R) \\
&\times \psi_{\mathrm{VR}}(x, y, L_z + z, R)\psi_{\mathrm{VR}}(x, y, -L_z + z, R),
\end{aligned} \tag{2.5}$$

where L_x, L_y and L_z are the extents of the computational grid in each dimension. After placing the two rings of a pair, they can be shifted by a random offset $\vec{w}$ by multiplying by $\exp(\mathrm{i}\vec{k} \cdot \vec{w})$ in Fourier space.

The spectrum of the RVR initial state with $N_{\mathrm{v}} = 800$, $R_{\mathrm{v}} = L/4$ on a grid of extents $L = L_x = L_y = L_z = 512$ and subsequent times is pictured in Figure 2.5. The amount of particles in the UV tail is noticeably smaller than for the box initial condition which uses the same simulation parameters. When taking a more precise look at the condensate mode in Figure 2.6, one can observe that there seems to be

a transition between the NTFP found from the box initial condition at early times and a faster (anomalous) scaling at later times. Also the total amount of particles in the condensate is at least an amplitude smaller compared to both of the box initial states at the same times. Fitting the spectra yields the exponents

$$\alpha = 1.61 \pm 0.10, \qquad \beta = 0.55 \pm 0.07, \qquad 200 \leq \frac{t}{2m\xi^2/\hbar} \leq 800 \qquad (2.6)$$

in the early time interval and

$$\alpha = 2.38 \pm 0.11, \qquad \beta = 0.82 \pm 0.05, \qquad 800 < \frac{t}{2m\xi^2/\hbar} \leq 6400 \qquad (2.7)$$

in the late time interval. The rescaled spectra for both time intervals can be found in Figure 2.7.
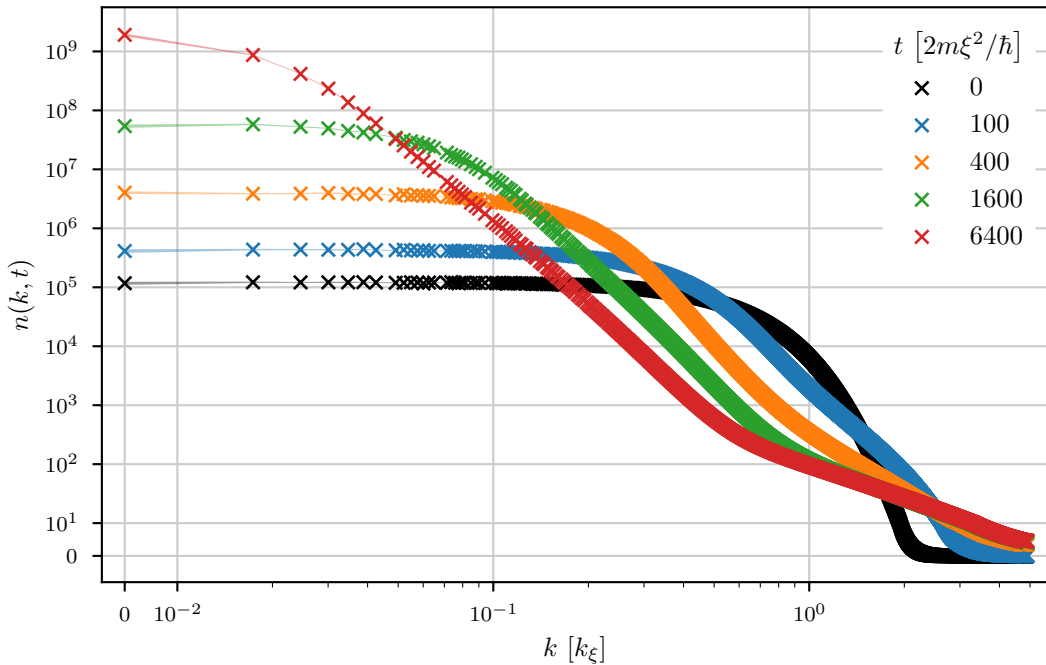

Figure 2.5: Angle-averaged occupation number spectrum of the RVR initial state at logarithmically spaced times showing self-similar scaling. Both axes use logarithmic scales to visualize the scaling and power laws in momentum k but include a linear region around 0 to accommodate the condensate mode $k = 0$ and the empty UV-modes of the initial state. The error of n is estimated using bootstrap resampling and marked by a semi-transparent error band which is only visible as a line between the data points at low momenta.
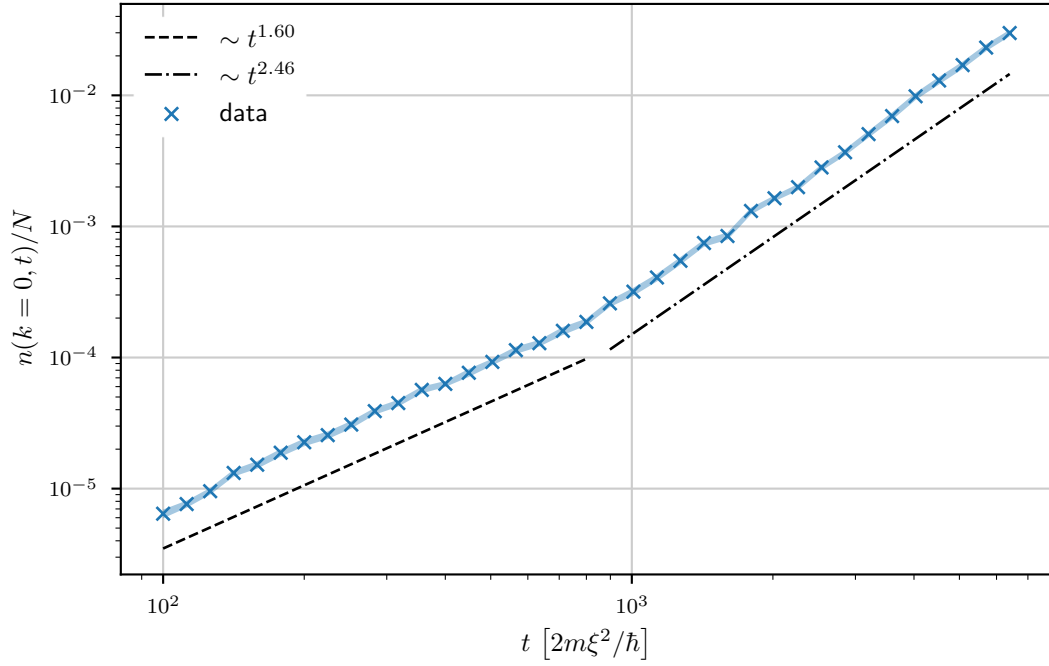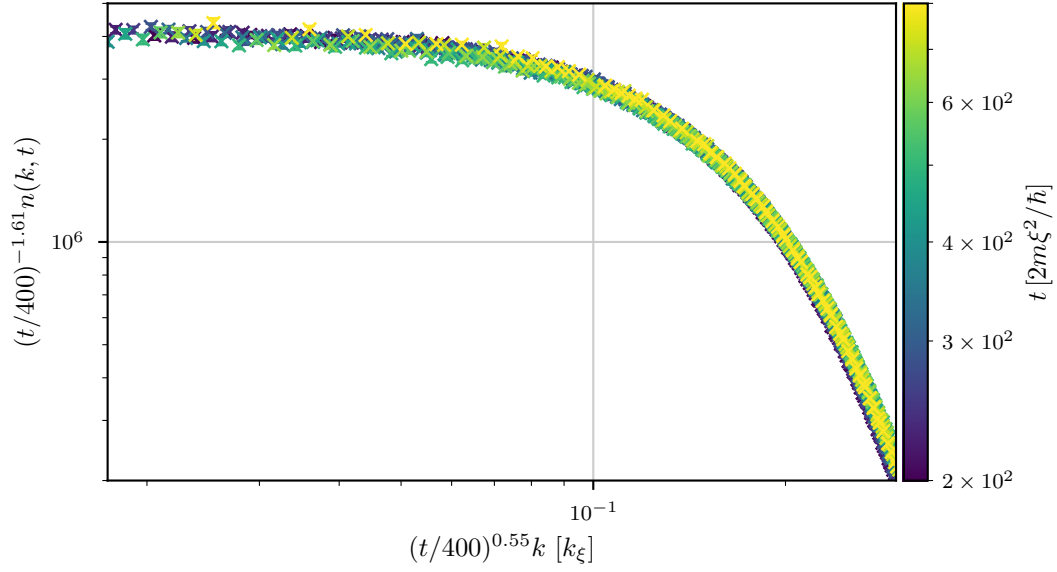
Figure 2.6: Occupation number of the condensate mode of the RVR initial state at logarithmically spaced times showing universal scaling with two different exponents. Both axes use logarithmic scales to visualize the scaling and power laws in time t. The error of $n(0,t)$ is estimated using bootstrap resampling and marked by a semi-transparent error band.

(a) early time interval
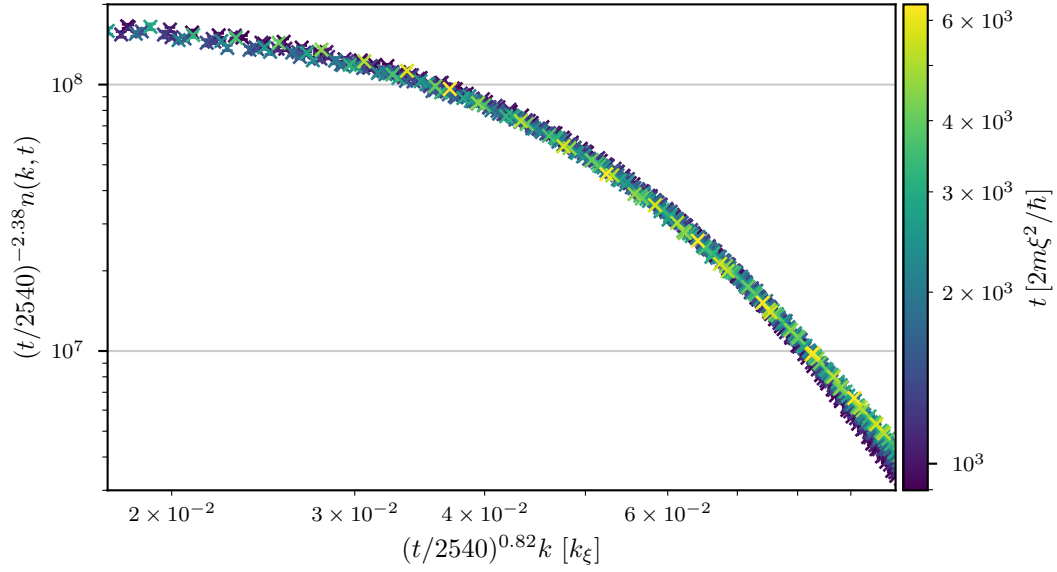
(b) late time interval

Figure 2.7: Log-log plot of the rescaled, angle-averaged occupation number spectrum in the momentum regions used for fitting the universal exponents at logarithmically spaced times in the early and late time interval simulated from the RVR initial state. The error of n is estimated using bootstrap resampling and marked by error bars.

3 Correlation Functions

In the absence of an external potential, translational and rotational invariance in position space are assumed for TWA-sampled observables on average. Therefore, any correlation function $C(\vec{x}, \vec{y})$ will be averaged over position space, yielding $C(\vec{y} - \vec{x}) \equiv C(\vec{r})$ and then over the solid angle, yielding $C(|\vec{r}|) \equiv C(r)$. Analogously the number density $\rho(\vec{x})$, which is used as normalization, will be averaged over position space because there is no inherent distance r to it. Due to numerical constraints, all spatial averages were taken before averaging over TWA-samples (of then one-dimensional observables) and calculating composite observables (e.g. normalization of correlation functions by ρ and calculating squares of 'normal' observables for connected correlation functions).

3.1 Full Correlation Functions

The normalized, Weyl-ordered 2-point correlation function

$$g^{(1)}(\vec{x}, \vec{y}, t) \equiv \frac{1}{\rho} \left\langle : \hat{\psi}^\dagger(\vec{x}, t)\hat{\psi}(\vec{y}, t) :_W \right\rangle \tag{3.1}$$

and the density-density (4-point) correlation function

$$g^{(2)}(\vec{x}, \vec{y}, t) \equiv \frac{1}{\rho^2} \left\langle : \hat{\psi}(\vec{x}, t)\hat{\psi}^\dagger(\vec{x}, t)\hat{\psi}(\vec{y}, t)\hat{\psi}^\dagger(\vec{y}, t) :_W \right\rangle, \tag{3.2}$$

are analogous to observables of the same names from earlier works such as Świsłocki and Deuar [2016].

As can be seen in Figure 3.1a, the field correlator $g^{(1)}$ mainly shows an exponential decay towards long distances r, with the rate of decay getting smaller over time, similar to the results reported in Schmied et al. [2019] for the spinor Bose gas. This signifies the growth of regions of similar phase $\theta(\vec{x})$ which will be confirmed in the following by the phase correlation functions. For early times, one can find some rather complex behavior at the end of the approximately exponential decay, which at later times is not observable anymore due to the finite size of the simulated volume. The existence of scaling behavior in the field correlations will be further discussed in the context of connected phase-angle correlators (subsection 3.2.2).

The density correlation function $g^{(2)}$ which can be seen in Figure 3.2 shows a lot less in terms of dynamics. While there is a drop in correlation which might be encompassing several different power laws at small distances r, for long distances the correlation function stays approximately at $\langle : \hat{\rho} :_W \rangle^2/\rho^2$, which is expected for

the thermalized Bose condensate. While there could be some scaling behavior in the power laws at small to intermediate distances, it is exceedingly hard to extract due to the thermal noise that is expected to be dominating at small distances and the very small range in which there seems to be a stable power law. As one clearly needs to rescale the data on both the ordinate and the abscissa to achieve overlap, one would also need to identify two power laws to try any systematic approach.

Moving on, the $2j$-point correlation function given by $\left(\hat{\psi}^\dagger(\vec{x},t)\hat{\psi}(\vec{y},t)\right)^j$ will be termed $g^{(1,j)}$, such that $g^{(1)} \equiv g^{(1,1)}$ and

$$g^{(1,j)}(\vec{x},\vec{y},t) \equiv \frac{1}{\rho^j} \left\langle : \left(\hat{\psi}^\dagger(\vec{x},t)\hat{\psi}(\vec{y},t)\right)^j :_W \right\rangle. \tag{3.3}$$

Only the 4-point correlation function $g^{(1,2)}$ will be shown at this point in Figure 3.1b, as the $g^{(1,j)}$, $j > 1$ on their own are visually very similar to the $g^{(1)}$. To investigate the effect of phase excitations on their own, analogous phase $\mathrm{e}^{\mathrm{i}\hat{\theta}(\vec{x},t)} \equiv \frac{\hat{\psi}(\vec{x},t)}{|\hat{\psi}(\vec{x},t)|}$ correlation functions are defined as

$$g_\theta^{(1,j)}(\vec{x},\vec{y},t) \equiv \left\langle : \left(\mathrm{e}^{\mathrm{i}\hat{\theta}(\vec{x},t)}\mathrm{e}^{-\mathrm{i}\hat{\theta}(\vec{y},t)}\right)^j :_W \right\rangle. \tag{3.4}$$

Because these phase correlation functions were visually indistinguishable from the respective full field correlation functions $g^{(1,j)}$, Figure 3.3 shows the 2- and 4-point phase correlation functions divided by their field correlation function counterparts. Apart from very small distances and times, the phase correlation functions encode the same spatial information as the field correlation functions.

3.2 Connected Correlation functions

Due to the U(1) symmetry of the system, the mean field $\langle\hat{\psi}(\vec{x},t)\rangle$ as well as any correlation functions containing unpaired bosonic field operators like $\langle\hat{\psi}(\vec{x},t)\hat{\psi}(\vec{y},t)\rangle$ or $\langle\hat{\psi}(\vec{x},t)\hat{\psi}^\dagger(\vec{x},t)\hat{\psi}(\vec{y},t)\rangle$ have to vanish as they are not invariant under global U(1)-transformations. In practice, however, they are nonzero due to finite size/finite sampling size effects. When taking them into account while calculating connected correlation functions, they can contribute significantly, especially when phase-ordering dynamics create long-range order over the whole computational grid. As can be seen in Appendix B, these contributions and their combinations, as they would be used for connected correlation functions, depend strongly on the number of samples while the full correlation functions do not. Therefore, these contributions will be disregarded in the following.

3.2.1 Connected 4-point Correlation Functions

Given the above considerations, the 2-point correlation function already corresponds to a connected correlation function $g_\mathrm{c}^{(1)} \equiv g^{(1)}$, while the connected 4-point functions
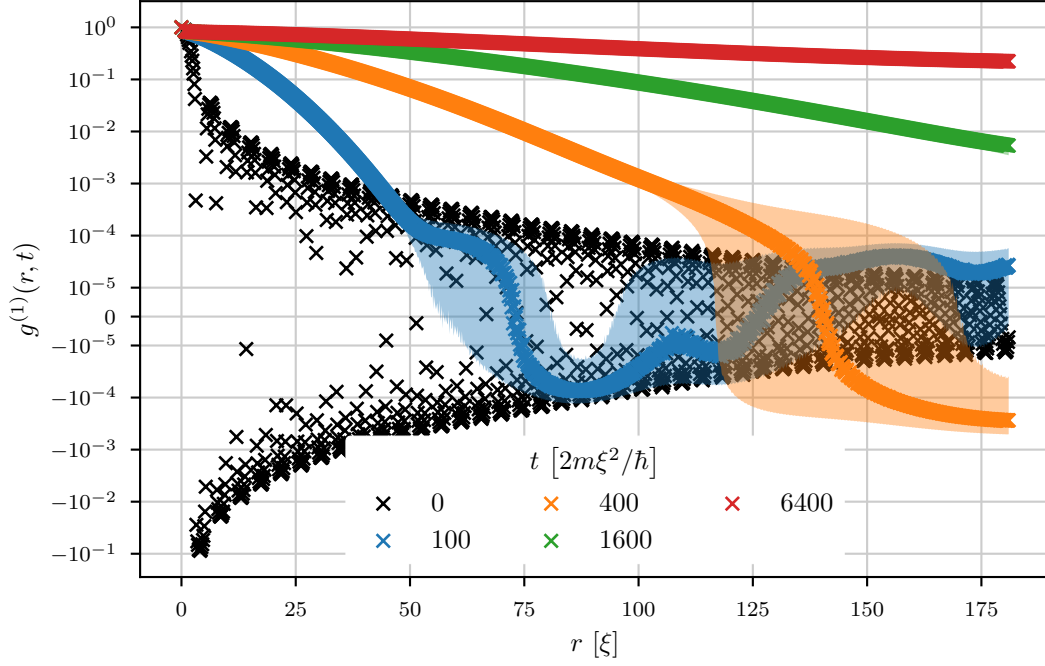
(a) 2-point correlation function
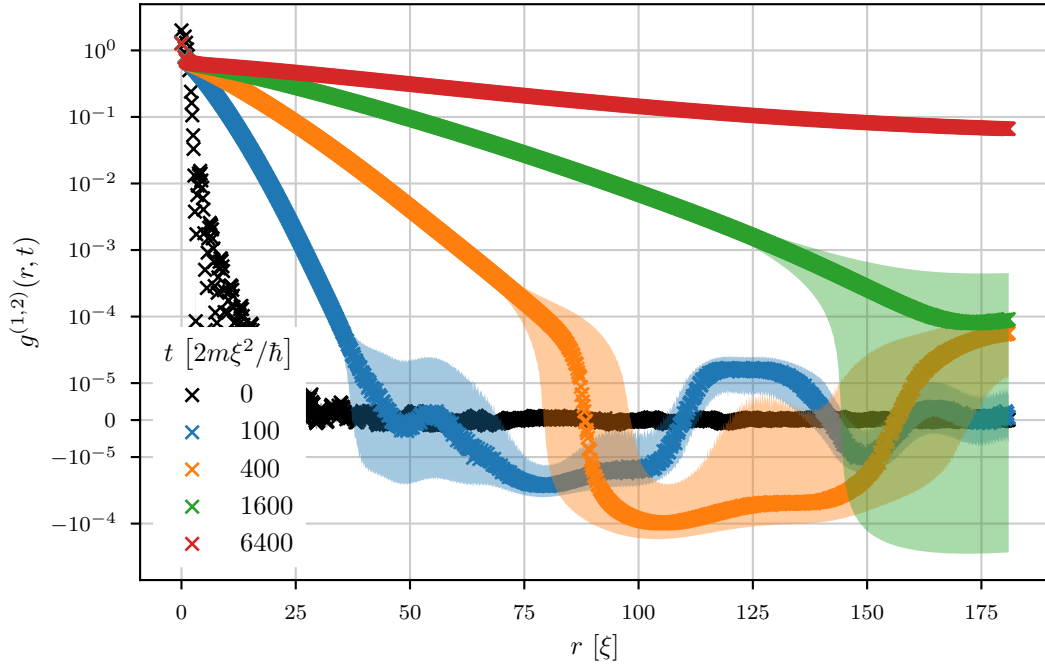
(b) 4-point correlation function

Figure 3.1: Normalized, angle-averaged 2- and 4-point field-field correlation functions of the box initial state with $k_{\text{cutoff}} = 1.4k_\xi$ and at logarithmically spaced times showing coarsening. To visualize the exponential decay, the ordinate uses a logarithmic scale up to a region around zero to accommodate negative values of the correlation functions while the abscissa (distance r) is using a linear scale. The errors of the correlation functions are estimated using bootstrap resampling and marked by a semi-transparent error band.
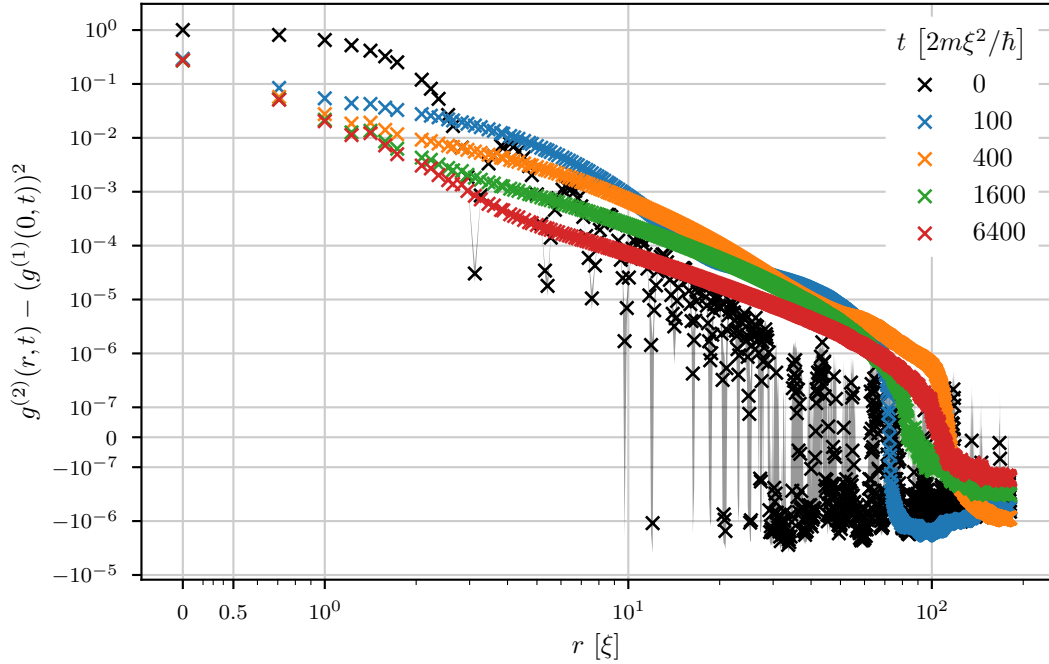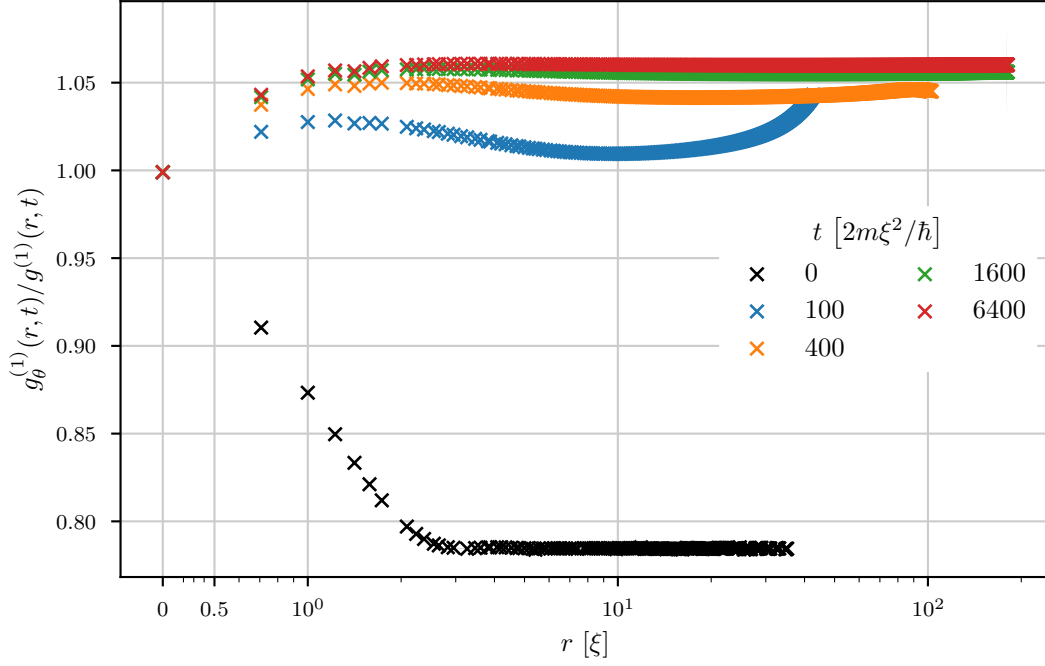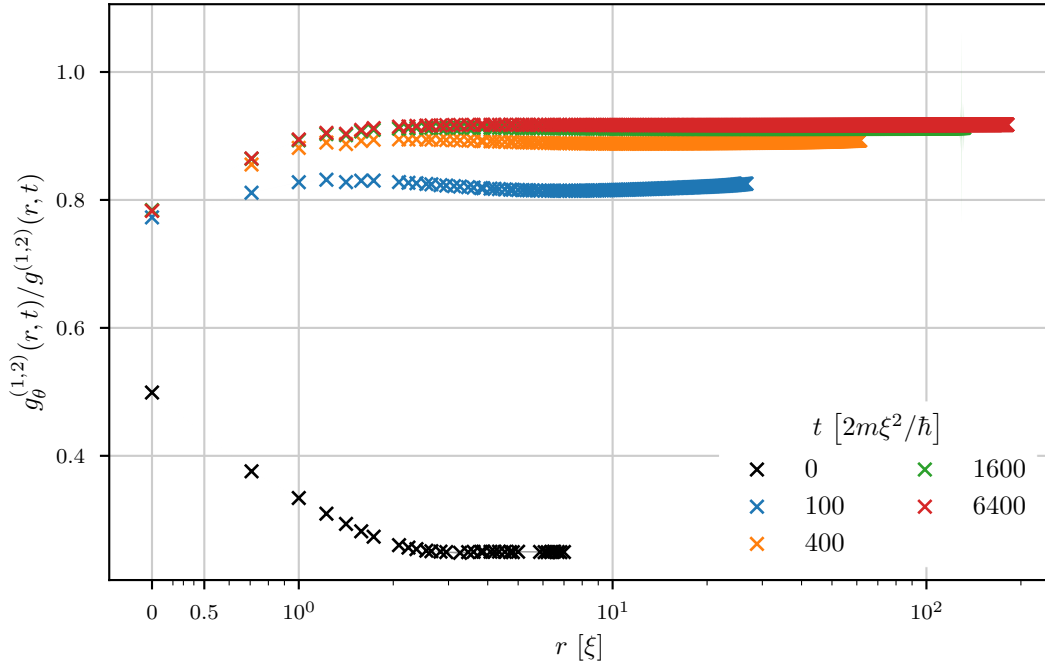
Figure 3.2: Normalized, angle-averaged density-density (4-point) correlation function of the box initial state with $k_{\text{cutoff}} = 1.4 k_\xi$ and at logarithmically spaced times. To focus on the (comparatively small) dynamics, all values were subtracted by the constant $(g^{(1)}(0,t))^2$ which can be evaluated to $(1 + 1/(2\rho))^2 \approx 1$ in the context of TWA on a discretized lattice. Both axes use a logarithmic scale up to a region around zero to accommodate $g^{(2)}(0,t) \equiv \langle\hat{\rho}^2\rangle/\langle\hat{\rho}\rangle^2$ and the correlator slightly undershooting $(g^{(1)}(0,t))^2$ at long distances r. The error of $g^{(2)}$ is estimated using bootstrap resampling and marked by a semi-transparent error band.

(a) 2-point correlation function ratio

(b) 4-point correlation function ratio

Figure 3.3: Ratio between the angle-averaged 2- and 4-point phase correlation functions and the 2- and 4-point field correlation functions of the box initial state with $k_{\text{cutoff}} = 1.4 k_\xi$ and at logarithmically spaced times. To focus on the dynamics mostly happening at small distances r, the abscissa uses a logarithmic scale up to a region around zero. The errors of the ratios are estimated using bootstrap resampling and marked by a semi-transparent error band. To avoid values with big errors, the ratios are only plotted at distances where $|g^{(1,j)}(r,t)| > 10^{-3}, j \in \{1, 2\}$.

are given by

$$g_c^{(2)}(\vec{r}, t) \equiv g^{(2)}(\vec{r}, t) - \left(g^{(1)}(\vec{r}, t)\right)^2 - \left(g^{(1)}(\vec{0}, t)\right)^2, \tag{3.5}$$

where $g^{(1)}(\vec{0}, t) \equiv \langle : \hat{\rho} :_W \rangle / \rho$ and

$$g_c^{(1,2)}(\vec{r}, t) \equiv g^{(1,2)}(\vec{r}, t) - 2 \left(g^{(1)}(\vec{r}, t)\right)^2. \tag{3.6}$$

Both connected 4-point correlators depicted in Figure 3.4 seem to be dominated by the $-(g^{(1)})^2$ contribution in their roughly exponential decay but look quite different at long distances, where already the $g^{(1)}$ showed some complex behavior. While the $-(g^{(1)})^2$ term naturally can not be positive, both connected correlators overshoot zero at different distances r. For comparison with the phase-angle correlators of the next section, Figure 3.5 shows minus the exponent of the decay of the two connected 4-point correlation functions. While they are very similar in form, the $-\log(-g_c^{(1,2)})$ flattens off more at short distances and is more consistent between different times in its slope at long distances.

3.2.2 Connected Phase-Angle Correlation Functions

An alternative way of arriving at connected correlation functions was inspired by Mikheev et al. [2019], where a low-energy effective field theory (EFT) for the U(N) models was proposed. The EFT is derived from the full theory by integrating out the density degree of freedom, as the density excitations are much more costlier in terms of energy than the phase excitations which are the Goldstone bosons of the U(1) symmetry and therefore massless. It should be mentioned here that the proposed EFT does not include (quasi-) topological excitations like vortex-lines and is therefore generally not expected to describe the numerical results in this thesis. However, the cited paper also makes use of the expansion of the generating functional of the EFT
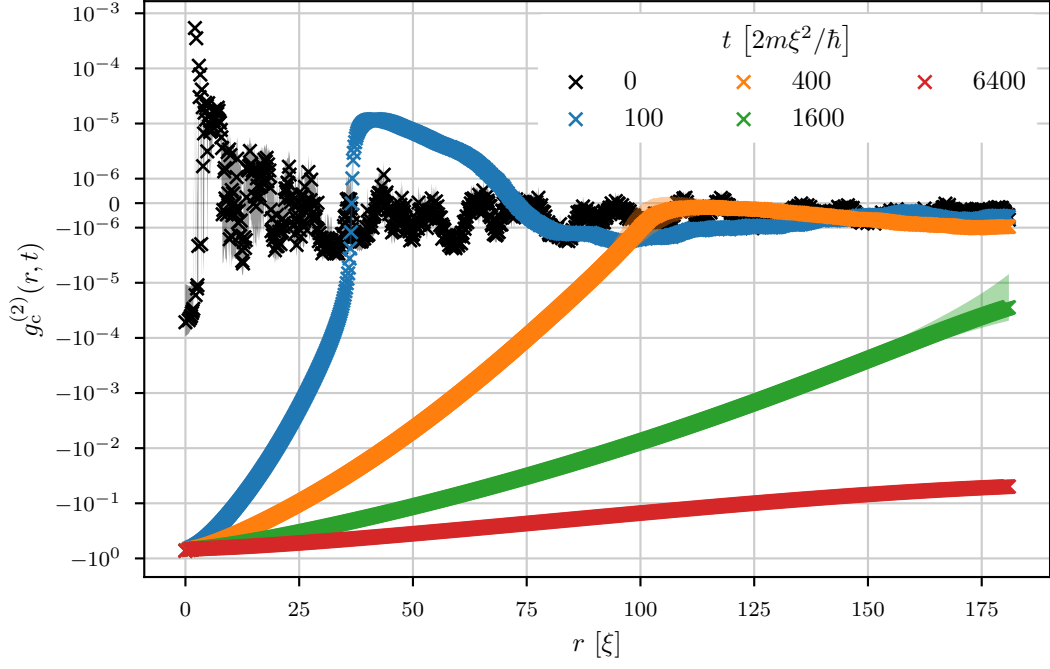
$$Z_{\text{eff}}[J] \equiv \int \mathrm{D}\theta \, \exp \left\{ \mathrm{i} S_{\text{eff}}[\theta] + \mathrm{i} \int_{x,C} J(x) \theta(x) \right\} \tag{3.7}$$

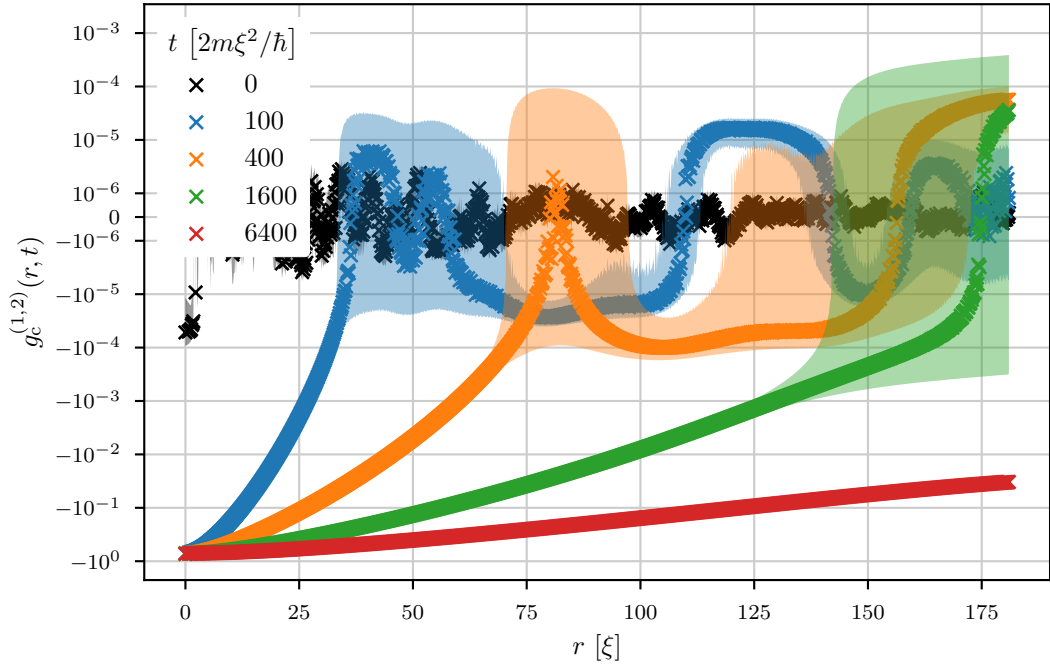in the connected n-point correlation functions functions $G^{(n)}$

$$Z[J] = \exp \left\{ \sum_{n=1}^{\infty} \int_{\{x_i\}_{i=1}^n, C} \frac{i^n}{n!} G^{(n)}(x_1, \ldots, x_n) J(x_1) \ldots J(x_n) \right\} \tag{3.8}$$

to relate the 2-point phase correlation function to connected phase-angle correlation functions $G_\theta^{(n)}(\vec{x}_1, \ldots, \vec{x}_n, t) = \langle \theta(\vec{x}_1, t) \ldots \theta(\vec{x}_n, t) \rangle_c$ without applying any functional derivatives. This is achieved by observing that for this special case, evaluating the generating functional with delta distributions as source terms gives phase correlation functions:

$$Z_{\text{eff}}[\{J = j[-\delta(\vec{x} - \vec{r}) + \delta(\vec{x})]\delta_C(x_0 - t), 0\}] = \int \mathrm{D}\theta \, (\mathrm{e}^{\mathrm{i}\theta(\vec{x},t)} \mathrm{e}^{-\mathrm{i}\theta(\vec{x}-\vec{r},t)})^j \mathrm{e}^{\mathrm{i} S_{\text{eff}}[\theta]}$$

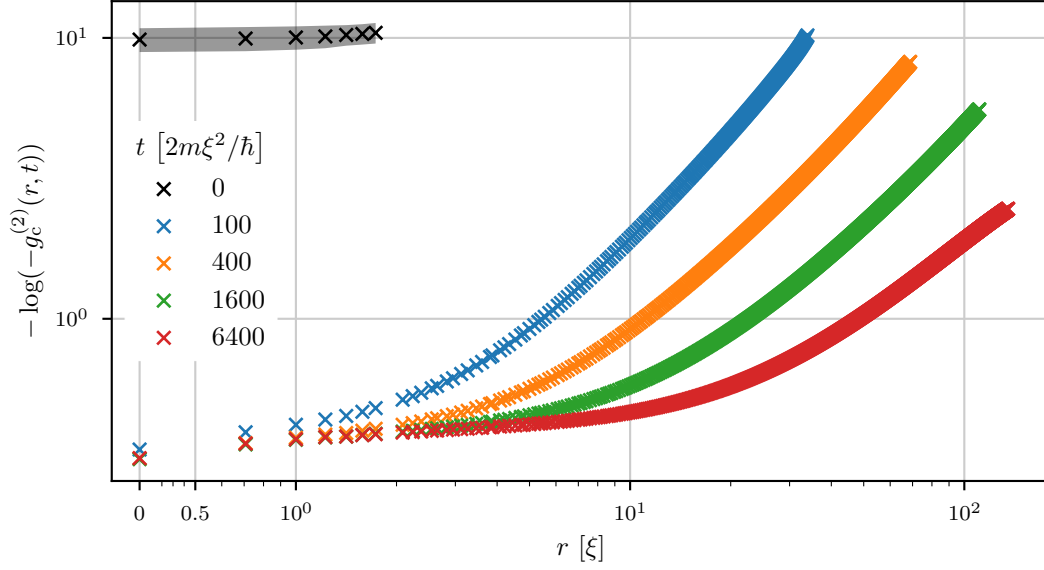$$= g_\theta^{(1,j)}(\vec{x}, \vec{x} - \vec{r}, t) \tag{3.9}$$
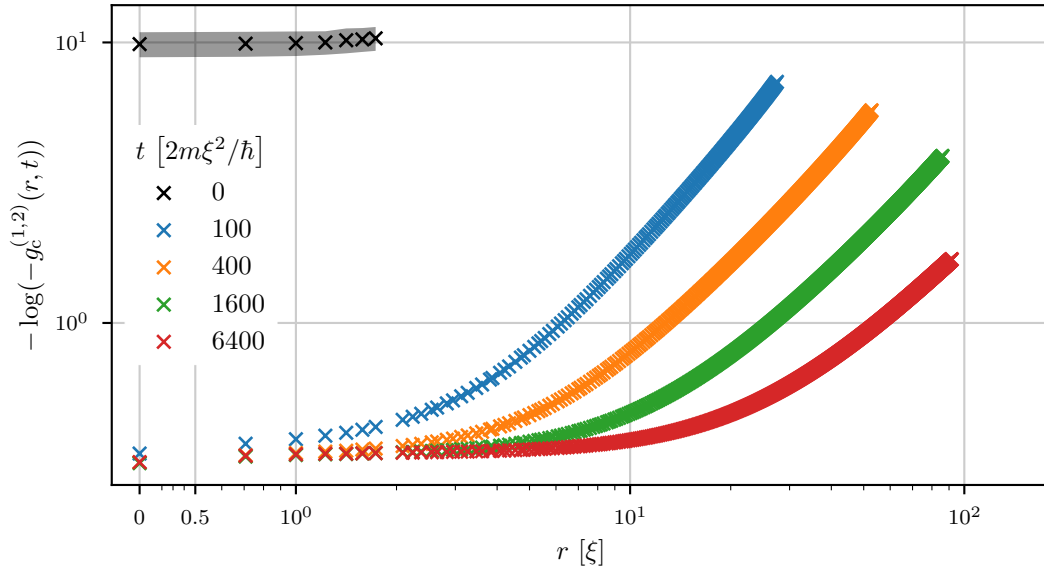
(a) Density correlation function

(b) Field correlation function

Figure 3.4: Normalized, angle-averaged connected 4-point density and field correlation functions of the box initial state with $k_{\mathrm{cutoff}} = 1.4k_\xi$ and at logarithmically spaced times showing coarsening. To visualize the exponential decay, the ordinates use logarithmic scales up to a region around zero to accommodate negative values of the correlation function while the abscissas (distance r) are using a linear scale. The error of the connected correlation functions is estimated using bootstrap resampling and marked by a semi-transparent error band.

(a) Density correlation function

(b) Field correlation function

Figure 3.5: Minus the logarithm of minus the angle-averaged connected 4-point density and field correlation functions of the box initial state with $k_{\text{cutoff}} = 1.4 k_\xi$ and at logarithmically spaced times showing universal scaling in r. For each time only distances up to the first r where the standard deviation of the respective correlation function grows bigger than its mean are used, stopping the evaluation before they turn negative. To visualize the different power laws in the exponent of the correlators, the ordinates use logarithmic scales while the abscissas (distance r) are using a logarithmic scale up to a region around zero. The error of the observables is estimated using bootstrap resampling and marked by a semi-transparent error band which is not visible due to its small size.

Evaluating Equation 3.8 for the same source term gives the following expansion:

$$g_\theta^{(1,j)}(\vec{x}, \vec{x} - \vec{r}, t) = \exp\left\{\sum_{n=1}^\infty j^n \frac{i^n}{n!} \mathcal{G}_\theta^{(n)}(\vec{r}, t)\right\}, \tag{3.10}$$

where the connected n-point phase-angle correlation functions were grouped into terms

$$\mathcal{G}_\theta^{(n)}(\vec{r}, t) \equiv \sum_{\vec{x}_1 \in \{\vec{0}, \vec{r}\}} \cdots \sum_{\vec{x}_n \in \{\vec{0}, \vec{r}\}} (-1)^{\sum_{i=1}^n \delta_{\vec{r}, \vec{x}_i}} G_\theta^{(n)}(\vec{x}_1, \ldots, \vec{x}_n, t). \tag{3.11}$$

The terms $\mathcal{G}_\theta^{(n)}(\vec{r}, t)$ combine Weyl ordered connected correlation functions

$$G_{\theta,\text{sym}}^{(n,q)}(\vec{r}, t) \equiv \left. \frac{(-i)^n \delta^n \log(Z[J])}{\delta^{n-q} J(\vec{0}, t)\, \delta^q J(\vec{r}, t)} \right|_{J=0}, \qquad q \in \{0, \ldots, n\} \tag{3.12}$$

in the following way:

$$\mathcal{G}_\theta^{(n)}(\vec{r}, t) = \sum_{q=0}^n (-1)^q \binom{n}{q} G_{\theta,\text{sym}}^{(n,q)}(\vec{r}, t). \tag{3.13}$$

Under translational and rotational invariance only even orders contribute, as for uneven n there is always two $G_\theta^{(n)}(\vec{x}_1, \ldots, \vec{x}_n, t)$ with $\vec{r} \leftrightarrow \vec{0}$ inverted position combinations cancelling each other out. This also can verified in Equation 3.13 by observing that $G_{\theta,\text{sym}}^{(n,q)}(\vec{r}, t) = G_{\theta,\text{sym}}^{(n,n-q)}(\vec{r}, t)$ and that for uneven n the sign of the q and $q' = n - q$ terms is opposite.

Given the observables $g_\theta^{(1,1)}, \ldots, g_\theta^{(1,j_{\max})}$, taking the logarithm on both sides of Equation 3.10 and approximating it by cutting off the expansion after $n_{\max} = 2j_{\max}$ orders, one gets a system of equations which can be solved for $\frac{(-1)^k}{(2k)!} \mathcal{G}_\theta^{(2k)}(\vec{r}, t)$ by (numerically) inverting the matrix $M = \{M_{j,k} = j^{2k} \mid j, k = 1, \ldots, j_{\max}\}$.

The resulting $\mathcal{G}_\theta^{(n)}$ for $j_{\max} = 4$, as well as the $\log(g_\theta^{(1,j)})$, of which they are linear combinations of, are pictured in Figure 3.6. The result is clearly consistent with regards to higher orders n of the expansion of $g_\theta^{(1)}$ being smaller than lower orders. While the leading order $\mathcal{G}_\theta^{(2)}$ is therefore almost identical with $-\log(g_\theta^{(1)})$, the higher orders show a power law reaching to much smaller distances r than the power law visible at the leading order. At the smallest distances a plateau is developing over time. While the power law of the leading order roughly translates to a linear exponent of the decay of the field correlation seen in the pure field correlation functions, the power law of higher orders n all correspond roughly to contributions quadratic in r.

One can naively exchange $g_\theta^{(1,n)}(\vec{r}, t)$ with field correlators

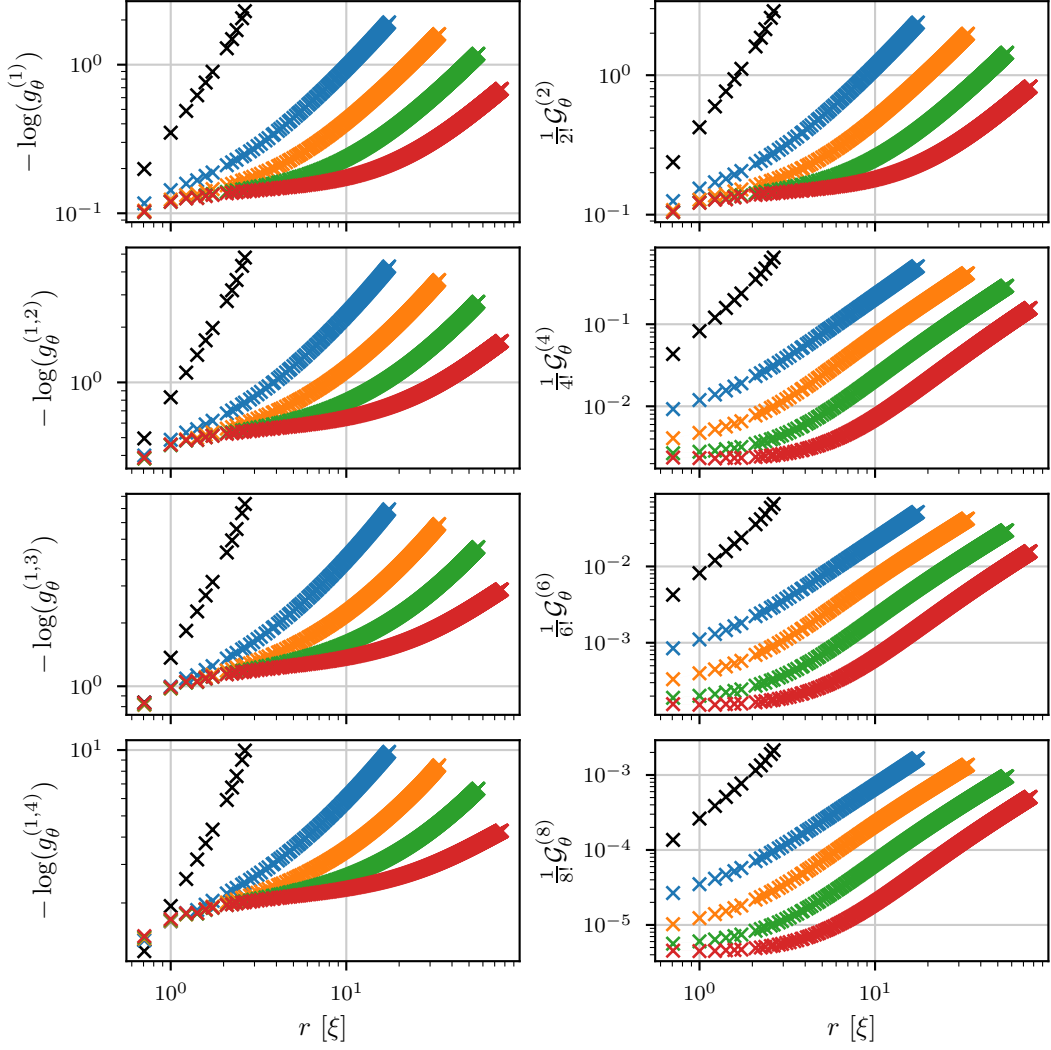$$g_\phi^{(1,j)}(\vec{r}, t) \equiv \frac{g^{(1,j)}(\vec{r}, t)}{g^{(1,j)}(\vec{0}, t)} \tag{3.14}$$

Figure 3.6: Log-log plots of minus the logarithm of the 2-, 4-, 6- and 8-point phase correlation functions $-\log(g_\theta^{(1,j)})$ on the left as well as the combinations of connected 2-, 4-, 6- and 8-point phase-angle correlation functions $\mathcal{G}_\theta^{(n)}$ on the right. Each connected correlation function on the right side is a linear combination of the four observables on the left side. The different colors correspond to the same logarithmically spaced times as in previous Figs. (black $t = 0$, blue $t = 100$, yellow $t = 400$, green $t = 1600$, red $t = 6400$, where t is given in characteristic time units $2m\xi^2/\hbar$). For each time only distances up to the first r where the standard deviation of any $g_{(\theta)}^{(1,j)}$ grows bigger than its mean are used, stopping the evaluation before they turn negative. Errors on both sides were estimated using bootstrap resampling and are marked using semi-transparent error bands which are not visible due to their small size. While the leading order $\mathcal{G}_\theta^{(2)}$ naturally shows the same behavior as $-\log(g_\theta^{(1)})$, the higher orders all show the same behavior with the visible power law reaching smaller distances r than the leading order.

28

and observe the difference in behavior due to density fluctuations. The different normalization is chosen to match $g_\theta^{(1,j)}(\vec{0}, t) \equiv 1$. However, to find a quantum field theoretic description of such an observable, one would need to devise a description in terms of the complex pseudo phase-angle $\phi(\vec{x}, t) \equiv \theta(\vec{x}, t) - \frac{i}{2} \log(\rho(\vec{x}, t))$. After seeing previously that the phase correlation functions $g_\theta^{(1,j)}$ and the field correlation functions $g^{(1,j)}$ seem to carry the same spatial information at intermediate and long distances r, it is not surprising that the $\mathcal{G}_\theta^{(n)}$ and $\mathcal{G}_\phi^{(n)}$ are very similar as well. The main difference visible in the plots is that the plateau at short distances of the $n > 2$ terms goes further and therefore the quadratic region is smaller when density fluctuations are included.
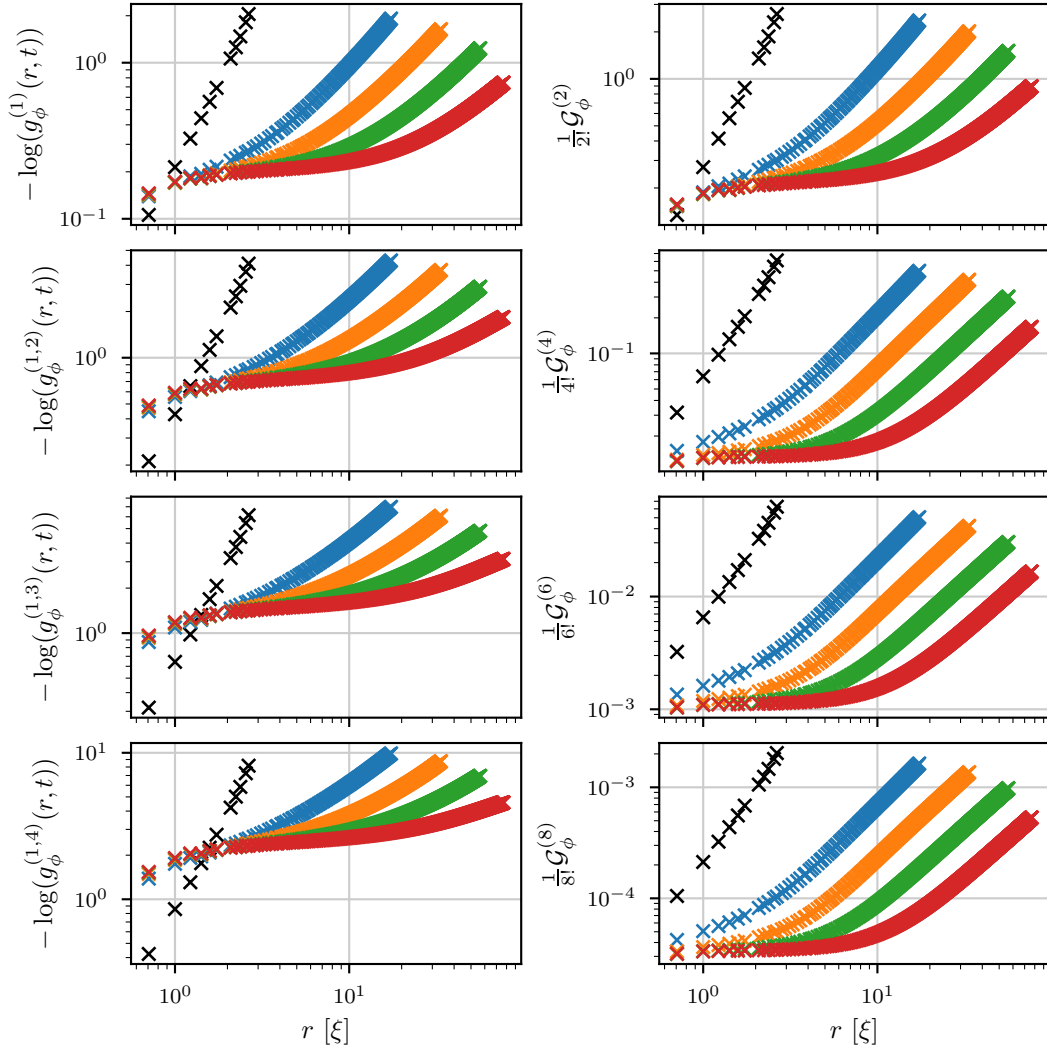
Figure 3.7: Log-log plots of minus the logarithm of the 2-, 4-, 6- and 8-point field correlation functions $-\log(g_\phi^{(1,j)})$ on the left as well as the combinations of connected 2-, 4-, 6- and 8-point phase-angle correlation functions $\mathcal{G}_\phi^{(n)}$ on the right. Each connected correlation function on the right side is a linear combination of the four observables on the left side. The different colors correspond to the same logarithmically spaced times as in previous Figs. (black $t = 0$, blue $t = 100$, yellow $t = 400$, green $t = 1600$, red $t = 6400$, where t is given in characteristic time units $2m\xi^2/\hbar$). For each time only distances up to the first r where the standard deviation of any $g_\phi^{(1,j)}$ grows bigger than its mean are used, stopping the evaluation before they turn negative. Errors on both sides were estimated using bootstrap resampling and are marked using semi-transparent error bands which are not visible due to their small size.

4 Conclusions and Outlook

Quenching a Bose gas far below its characteristic momentum scale results in dynamics that, due to oscillations in the scaling behavior, can lead to very small or very big exponents α and β. Due to the limited amount of times that can be inspected experimentally because of the destructive nature of quantum measurement, this is a possible explanation of the observation of small exponents in Glidden et al. [2021]. As the characteristics of the experimental cooling quench are not easily accessible from the information given in the paper, it is still possible that there is an actual anomalous NTFP causing the slow scaling in the experiment, which was not captured by the simulations due to the abstract nature of the used initial states. In the future one could try to produce more realistic data by simulating the cooling quench itself, instead of assuming its effect to be comparable with the effect of a box initial state.

By simulating a Bose gas with many big vortex rings at random positions and orientations as proposed by Kobayashi et al. [2021] as random vortex rings (RVR), fast anomalous scaling with $\beta \approx 0.8$ and $\alpha \approx 2.4$ was observed at late times. This new anomalous NTFP should be further investigated to find out how the dynamics differ exactly from the Gaussian NTFP. The fact that it appears after showing scaling compatible with the Gaussian NTFP, instead of before it, makes it even more interesting.

Comparing field and phase correlation functions, it was possible to confirm that almost all spatial information which encompasses the critical scaling is part of the phase field. Density fluctuations certainly also play an important role for the thermal background in the UV which allows vortex lines to shrink and vanish.

The very similar results of the two different connected 4-point correlation functions at intermediate distances might be seen as a sign of their correctness, but a physical interpretation of these results remains to be found. While it seems to be possible to extract β from these correlations, the result does not differ significantly from what was already extractable from full field correlation functions. Still, observables that allow the β to be determined independently from α could play an important role in future numerical research because it circumvents the problem that the IR plateau in the occupation number spectrum scales to momenta too small to be resolved on the computational lattice which in turn makes it impossible to determine the critical exponents independently from the spectra.

The connected phase-angle correlation functions that were extracted indirectly should be compared to directly computed phase-angle correlation functions to check the validity of assuming an EFT in the phase-angle despite the presence of vortex lines.

Part I

Appendix

A Numerical Solution of the GPE

A.1 Dimensionless GPE

Given an arbitrary length scale ℓ, we can define the following dimensionless variables and constants:

$$\vec{\bar{x}} \equiv \frac{\vec{x}}{\ell}, \qquad \bar{t} \equiv \frac{\hbar}{2m\ell^2}t,$$

$$\bar{\psi}(\vec{\bar{x}}, \bar{t}) \equiv \ell^{3/2}\psi(\vec{x}, t), \qquad \bar{V}(\vec{\bar{x}}) \equiv \frac{2m\ell^2}{\hbar^2}V(\vec{x}), \qquad \bar{g} \equiv \frac{2m}{\ell\hbar^2}g = 8\pi\bar{a}_S. \tag{A.1}$$

After substituting these in eq. 1.12, dividing by $\frac{\hbar^2}{2m\ell^2}$ and dropping the bar from the dimensionless variables and constants one gets the dimensionless GPE:

$$i\partial_t\psi(\vec{x}, t) = \left(-\vec{\nabla}^2 + V(\vec{x}) + g\left|\psi(\vec{x}, t)\right|^2\right)\psi(\vec{x}, t). \tag{A.2}$$

In this thesis all shown numerical results used the following numerical parameters:

$$N = 64 \times 10^9, \quad \bar{g} = 0.00104858, L = 512, \quad \Delta\bar{t} = 0.05, \tag{A.3}$$

where L is the extent of the numerical lattice in all three directions, s.t. the simulated volume is $\bar{V} = L^3$, and $\Delta\bar{t}$ is the step size in numerical time units.

A.2 Position Discretization

The length scale ℓ is chosen as the lattice spacing of the numerical lattice. The discretization in position space is therefore $\vec{x}_{\vec{j}} = \sum_i(j_i \mod L_i)e_i$, where $\vec{j}$ is the three-vector of indices, L_i is the number of vertices on the lattice in ith direction and e_i are the basis vectors. The modulo operation comes into play due to the nature of the split-step Fourier algorithm which assumes periodic boundary conditions as described in section A.5.

In the following, $\psi_j \equiv \psi(\vec{x}_{\vec{j}})$ is used as a shorthand. Furthermore, it makes sense to define the discrete Fourier transform (DFT) as

$$\Phi_{\vec{q}} = \frac{1}{\sqrt{L}}\sum_{\vec{j}}^{L_i}\psi_j e^{i2\pi\vec{q}\vec{j}/L_i}. \tag{A.4}$$

A.3 Momentum Discretization

The momentum space discretization is chosen to enforce the periodic lattice dispersion relation:

$$\hat{k}^2 \psi_j = -\nabla^2 \psi_j \approx -(\psi_{j+1} - 2\psi_j + \psi_{j-1}) \tag{A.5}$$

$$= \frac{1}{\sqrt{L}} \sum_{q=0}^{L} \psi_q \, e^{-i2\pi qj/L} 4 \sin^2(\pi q/L). \tag{A.6}$$

This choice implicitly sets the maximum absolute numerical momentum to $2\sqrt{3}$ (See section A.3), as numerical momentum takes values between -2 and 2 in each dimension.

A.4 Time Discretization

Starting from the formal solution $\psi(t) = U(t, t_0)\psi(t_0)$ with

$$U(t, t_0) = \mathcal{T} \exp\left(-i \int_{t_0}^{t} dt' \, \mathcal{K}(t')\right), \tag{A.7}$$

where $\mathcal{T}$ is the time-ordering operator and $\mathcal{K}$ corresponds to the 'Hamiltonian' of the GPE defined in section 1.2, one arrives at the basic numerical ansatz by discretizing time:

$$U(t, t_0) = \mathcal{T} \prod_{s=0}^{N_t} \exp\left(-i\Delta t \mathcal{K}(t_s)\right) \equiv \mathcal{T} \prod_{s=0}^{N_t} U(t_s) \tag{A.8}$$

A.5 Split-Step Fourier Method

To solve the Gross-Pitaevskii equation numerically while conserving the number of particles, the pseudo-spectral Split-Step Fourier method is used. The ansatz of explicitly calculating the discretized time evolution operator $U(t_s)$ is modified by splitting $\mathcal{K}$ into operators that are diagonal in position space $\mathcal{K}_{\text{pos}}$ like an external potential and the non-linear interaction term and ones that are diagonal in momentum space $\mathcal{K}_{\text{mom}}$ like the kinetic term:

$$e^{-i\Delta t \mathcal{K}} = e^{-i\Delta t \mathcal{K}_{\text{mom}}} e^{-i\mathcal{K}_{\text{pos}}} + \mathcal{O}(\Delta t^2) \tag{A.9}$$

Now one can use a DFT to transform the state ψ between position basis and momentum basis such that the operators become diagonal and therefore the matrix exponential becomes an element-wise exponential. By using the Fast-Fourier-Transform (FFT) algorithm, the DFTs can be computed very efficiently with $\mathcal{O}(\mathcal{N} \log \mathcal{N})$ computational complexity and on modern (massively) parallel computer hardware

using the FFTW and CUFFT implementations. For solving the Gross-Pitaevskii equation to $\mathcal{O}(\Delta t^2)$ without significantly increasing numerical complexity, This naive algorithm can be improved upon by introducing half steps [Javanainen and Ruostekoski, 2006]:

$$\mathrm{e}^{-\mathrm{i}\Delta t\mathcal{K}} = \mathrm{e}^{-\mathrm{i}\frac{\Delta t}{2}\mathcal{K}_{\mathrm{mom}}}\mathrm{e}^{-\mathrm{i}\mathcal{K}_{\mathrm{pos}}}\mathrm{e}^{-\mathrm{i}\frac{\Delta t}{2}\mathcal{K}_{\mathrm{mom}}} + \mathcal{O}(\Delta t^3). \tag{A.10}$$

As one normally only analyzes snapshots of the system many numerical time steps apart, one can in practice fuse the momentum space half steps of different time steps to arrive at an algorithm which only has half steps at the beginning and end of time integration while the bulk of steps is done in the same fashion as for the $\mathcal{O}(\Delta t^2)$ algorithm.

B Finite Size / Finite Sampling Size Effects

As can be seen in Figure B.1, unphysical observables change significantly with the amount of TWA samples while physical ones show no such behavior that would have to be canceled out in a connected correlation function. While at early times the regions of coherent phase are so small that averaging over the simulation volume already reduces observables dependent on the mean field to very small values, they grow so big at late times that many more TWA-samples are needed to keep these observables insignificant.
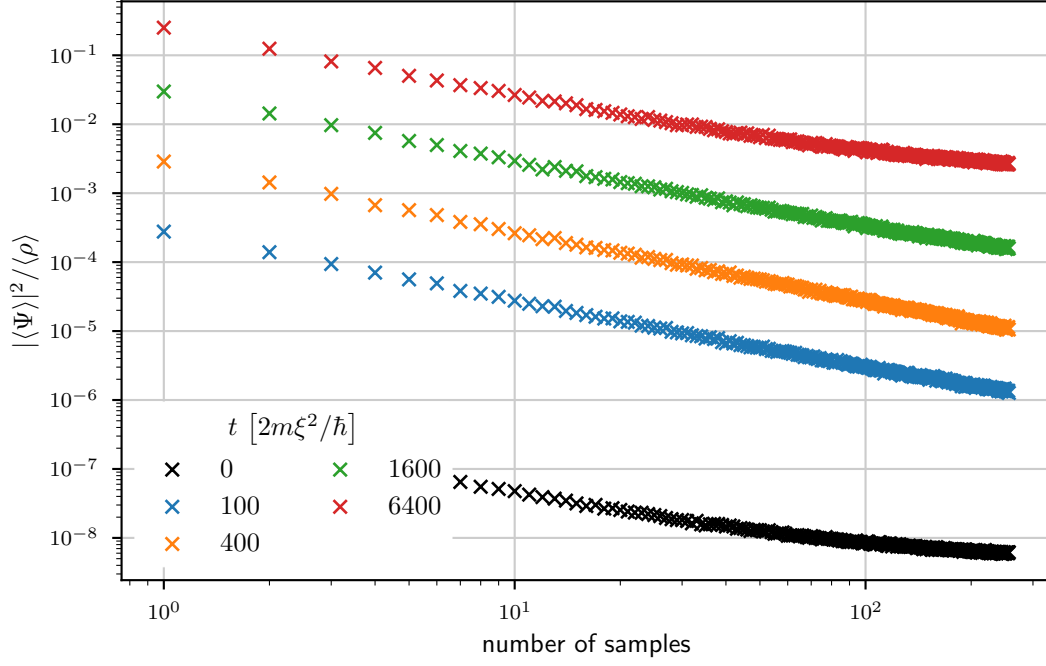
(a) Norm of the mean field
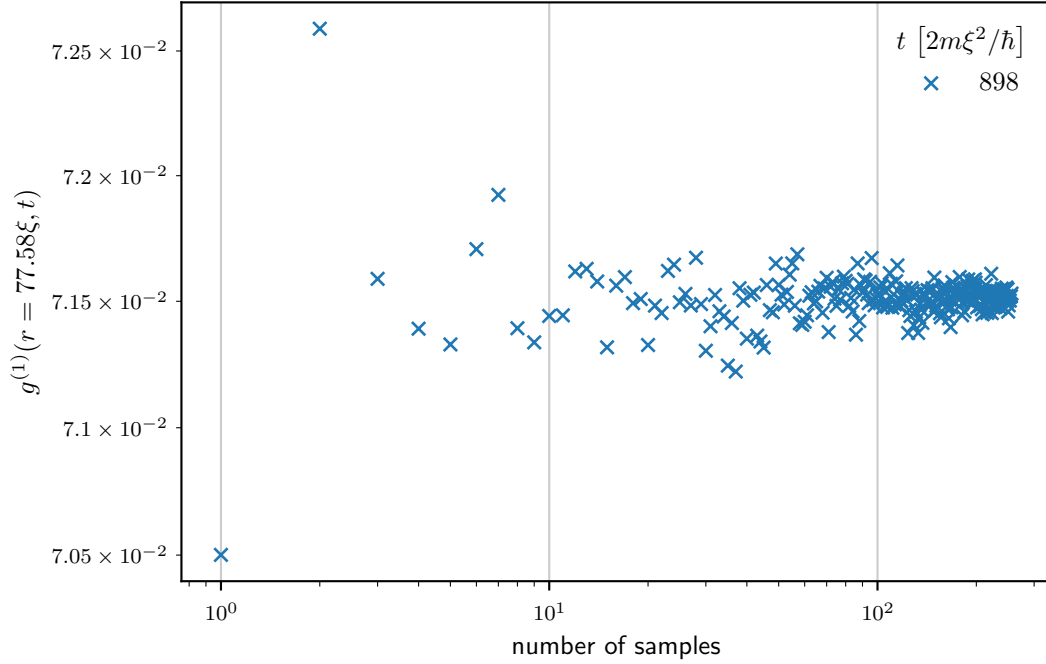
(b) 2-point field correlation function at an arbitrary time and distance

Figure B.1: Examples of how the mean field which should vanish due to the U(1) symmetry grows over time, while decreasing with an increasing amount of TWA-samples, while an arbitrary observable that is independent of global phase rotations shows no trend at all with an increasing amount of TWA-samples.

C Lists

C.1 List of Figures

D Bibliography

J. A. P. Glidden, C. Eigen, L. H. Dogra, T. A. Hilker, R. P. Smith, and Z. Hadzibabic. Bidirectional dynamic scaling in an isolated Bose gas far from equilibrium. *Nature Physics*, 17(4):457–461, January 2021. doi: 10.1038/s41567-020-01114-x.

E. P. Gross. Structure of a quantized vortex in boson systems. *Nuovo Cim.*, 20:454, May 1961.

J. Javanainen and J. Ruostekoski. Symbolic calculation in development of algorithms: split-step methods for the Gross–Pitaevskii equation. *Journal of Physics A: Mathematical and General*, 39(12):L179–L184, March 2006. doi: 10.1088/0305-4470/39/12/L02.

S. P. Johnstone, A. J. Groszek, P. T. Starkey, C. J. Billington, T. P. Simula, and K. Helmerson. Evolution of large-scale flow from turbulence in a two-dimensional superfluid. *Science*, 364(6447):1267–1271, 2019. ISSN 0036-8075. doi: 10.1126/science.aat5793. URL https://science.sciencemag.org/content/364/6447/1267.

M. Karl and T. Gasenzer. Strongly anomalous non-thermal fixed point in a quenched two-dimensional Bose gas. *New J. Phys.*, 19(9):093014, 2017. doi: 10.1088/1367-2630/aa7eeb. URL http://stacks.iop.org/1367-2630/19/i=9/a=093014.

M. Kobayashi, P. Parnaudeau, F. Luddens, C. Lothodé, L. Danaila, M. Brachet, and I. Danaila. Quantum turbulence simulations using the Gross-Pitaevskii equation: High-performance computing and new numerical benchmarks. *Computer Physics Communications*, 258:107579, January 2021. doi: 10.1016/j.cpc.2020.107579.

A. N. Mikheev, C.-M. Schmied, and T. Gasenzer. Low-energy effective theory of nonthermal fixed points in a multicomponent Bose gas. *Phys. Rev. A*, 99(6):063622, 2019. doi: 10.1103/PhysRevA.99.063622.

B. Nowak, J. Schole, and T. Gasenzer. Universal dynamics on the way to thermalisation. *New J. Phys.*, 16:093052, September 2014. doi: 10.1088/1367-2630/16/9/093052.

A. Piñeiro Orioli, K. Boguslavski, and J. Berges. Universal self-similar dynamics of relativistic and nonrelativistic field theories near nonthermal fixed points. *Phys. Rev. D*, 92(2):025041, 2015. doi: 10.1103/PhysRevD.92.025041.

L. P. Pitaevskii. Vortex lines in an imperfect Bose gas. *Sov. Phys. JETP*, 13:451, 1961.

A. Polkovnikov. Phase space representation of quantum dynamics. *Ann. Phys.*, 325 (8):1790, 2010. doi: 10.1016/j.aop.2010.02.006.

M. Prüfer, P. Kunkel, H. Strobel, S. Lannig, D. Linnemann, C.-M. Schmied, J. Berges, T. Gasenzer, and M. K. Oberthaler. Observation of universal quantum dynamics far from equilibrium. *Nature*, 563(7730):217–220, 2018. doi: 10.1038/s41586-018-0659-0.

C.-M. Schmied, M. Prüfer, M. K. Oberthaler, and T. Gasenzer. Bidirectional universal dynamics in a spinor Bose gas close to a nonthermal fixed point. *Phys. Rev. A*, 99:033611, Mar 2019. doi: 10.1103/PhysRevA.99.033611. URL https://link.aps.org/doi/10.1103/PhysRevA.99.033611.

M. J. Steel, M. K. Olsen, L. I. Plimak, P. D. Drummond, S. M. Tan, M. J. Collett, D. F. Walls, and R. Graham. Dynamical quantum noise in trapped Bose-Einstein condensates. *Phys. Rev. A*, 58(6):4824, Dec 1998. doi: 10.1103/PhysRevA.58.4824.

T. Świsłocki and P. Deuar. Quantum fluctuation effects on the quench dynamics of thermal quasicondensates. *Journal of Physics B Atomic Molecular Physics*, 49 (14):145303, July 2016. doi: 10.1088/0953-4075/49/14/145303.

Erklärung:

Ich versichere, dass ich diese Arbeit selbstständig verfasst habe und keine anderen als die angegebenen Quellen und Hilfsmittel benutzt habe.

Heidelberg, den 1. Oktober 2021